Chapter 8

Boundary Layer Survey

The location of laminar to turbulent transition of the boundary layer, as estimated from the surface pressure measurements, appears to shift significantly between the lowest and highest Reynolds numbers tested. In a few cases the flow visualisation also provides indications of boundary layer transition. More definitive measurements of the boundary layer state are desirable given the importance of the boundary layer state to the overall flow. To perform these measurements a three-dimensional traversing system and a fast response total pressure probe (FRTPP) were designed and manufactured. In addition, methods were implemented to enable both accurate determination of the model position and examination of the boundary layer state.

8.1 Three-Dimensional Traverse System

The three-dimensional automated traverse has interchangeable probe supports and is capable of operating over the full pressure and velocity range of the tunnel. The traverse is mounted on a $46\,mm$ thick stainless steel plate that may be placed in any of the six side window frames of the tunnel test section. The main traverse window has a $225\,mm$ square opening that allows access for the probe. The probe is held in position by the traversing plate. This plate can slide $\pm 100\,mm$ vertically from the centre-line of the tunnel on two sets of linear bearings. The rails that allow the plate to move vertically are indirectly attached to another set of linear bearings that allow the traversing plate to move $\pm 100\,mm$ horizontally from the centre of the window. An o-ring around the edge of the $225\,mm$ opening in the main traverse window provides a seal between the two plates. The traversing plate is large enough that the o-ring around the opening in the main plate is always covered.

The traversing plate is sandwiched between the main traverse window and a $100\,mm$ thick steel support frame designed to minimise the deflection of the traversing plate and the main

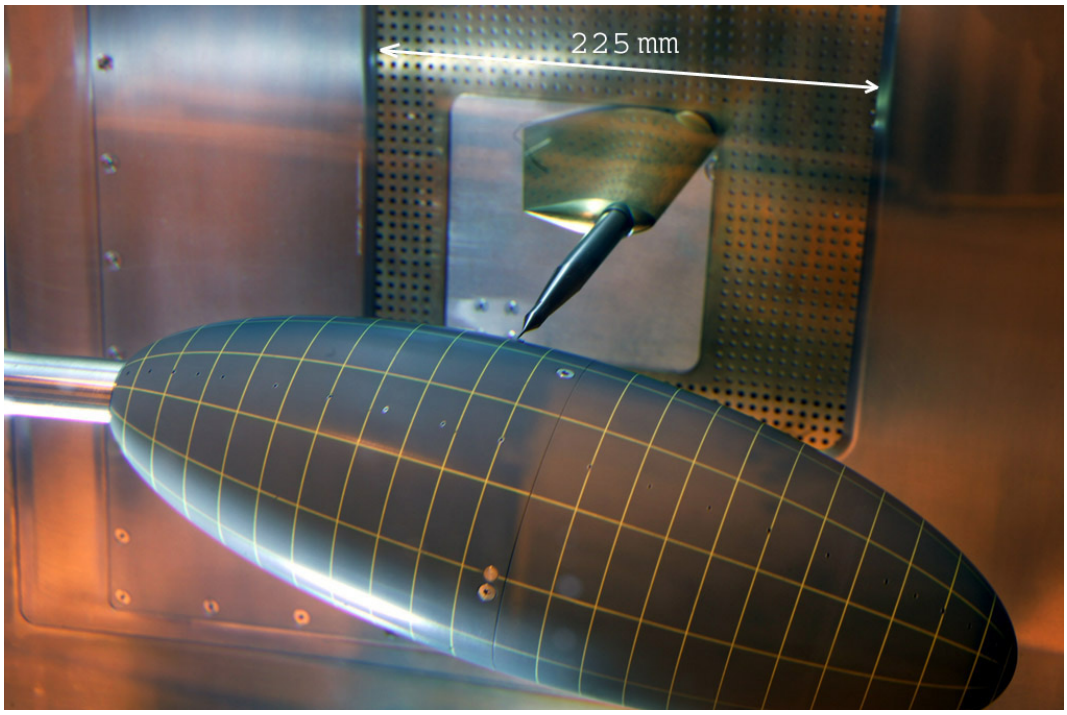

Figure 8.1: Traverse Interior

traverse window when the tunnel is pressurised. The traversing plate consists of a central stainless-steel plate with Teflon adhered to both sides. The area of Teflon contacting the steel support frame is optimised to reduce friction. The traversing window/support frame interface is subjected to approximately four times the loading of the traversing window/main traverse window interface when the tunnel is at its maximum and minimum pressures respectively. The optimisation of the contact area of the Teflon ensured that at maximum tunnel pressure the pressure on the Teflon is approximately $3\,N/mm^2$; below this pressure the coefficient of friction for Teflon increases significantly. A series of thin plates on the inside of the traverse keep the flow around the traversing mechanism streamlined (Fig. 8.1). The third axis allows the probe to be driven up to $300\,mm$ perpendicular to the traversing plate. A hydrofoil-section support is used to minimise probe vibration when the probe is inserted more than $150\,mm$ from the side of the tunnel. Appendix F shows diagrams of the traverse.

The traverse is controlled by a closed loop system. Movement of the vertical and horizontal axes of the traverse is achieved using Frame-34 stepper motors and fine-pitched roller screws. The fine-pitch roller screws allow these axes to be positioned accurately and with sufficient force to move the traverse when the tunnel is fully pressurised. A smaller Frame-17 stepper motor drives the probe attached to the traversing window. Linear position transducers measure the position of all axes. These measurements are read by the controller and used to move

the axes until the desired position is reached. The resolution of the traverse in all axes is $0.02\,mm$, with a positional accuracy of better than $0.1\,mm$ under most conditions. A remote control for the traverse has been developed to allow points on the surface of the model to be measured efficiently. These points are used to determine the position of the model in traverse coordinates. A new top window was designed and manufactured, that in combination with the original window allows a model to be positioned in $150mm$ increments between $x_t = \pm 750mm$.

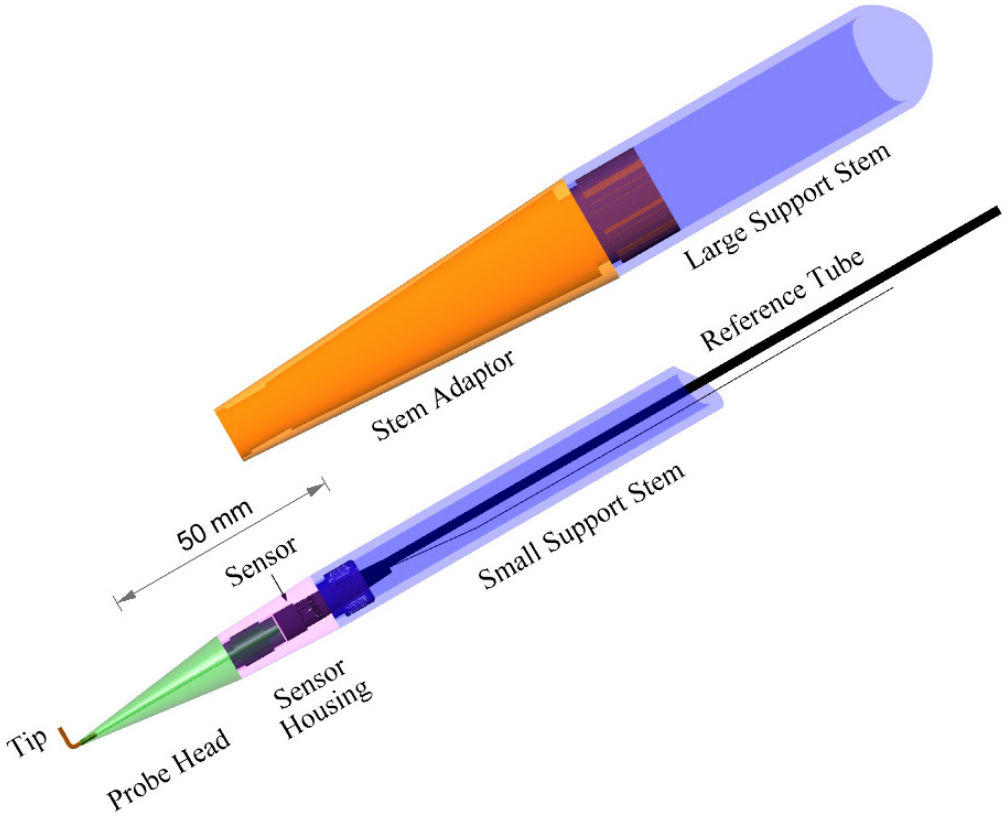

Figure 8.2: FRTPP general arrangement.

8.2 Fast Response Total Pressure Probe

The fast response total pressure probe (FRTPP) measures the total head with a miniature differential pressure sensor close to the tip. Placing the sensor close to the tip increases the frequency response of the probe. This probe is similar to those used in transonic [70] and combusting [71] flow applications. The FRTPP is designed to be modular. It consists of a number of sections as shown in Fig. 8.2. Each section can be changed to suit the flow being measured. The FRTPP with a $1.2mm$ diameter tip and 1.5 bar sensor is detailed in Brandner et al. [72]; in this paper its performance is compared against a hot film probe. For measurements of

intermittency a calibration is not required; however, its sensitivity was monitored with regular checks in the freestream. For the measurements around the spheroid at an incidence of $-10°$ a $1.0\,mm$ outside diameter (OD) tip was used. For all subsequent tests a $0.7\,mm$ OD tip was used. The probe used for the spheroid was otherwise as detailed in Brandner et al. [72]. The miniature differential pressure sensor has a reference port that requires a non-conducting non-corrosive medium. In order to use the tunnel static pressure as the reference a wet-dry interface was manufactured with air on the dry side. This interface also acted as a filter so that only lower frequency fluctuations (less than $10\,Hz$) in the tunnel static pressure would appear on the reference side of the sensor.

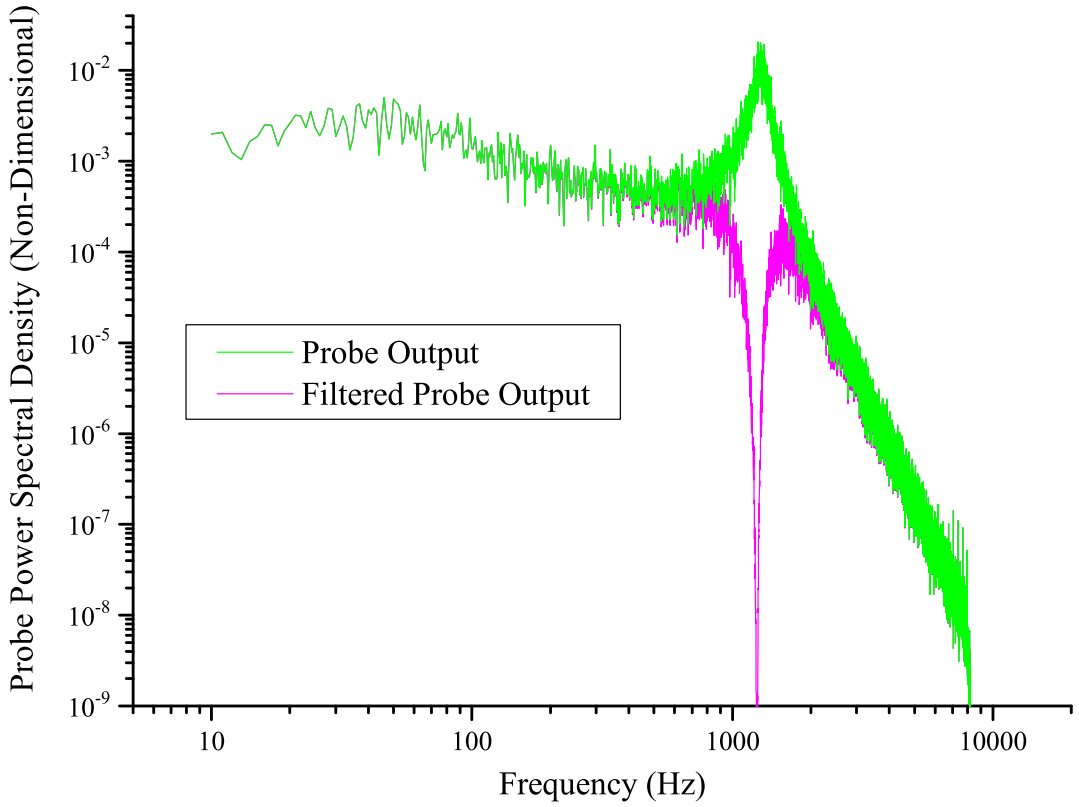

Figure 8.3: Frequency response of FRTPP with $0.7\,mm$ diameter tip at $Re_l = 2.0 \times 10^6$ as used for boundary layer survey on spheroids at $-0.2°$ and $-6.2°$. Output non-dimensionalised using freestream dynamic pressure and a unity period.

The output of the probe has a natural frequency that is a function of the tube dimensions and the stiffness of the probe sensor. The resonance peak due to this natural frequency is filtered, as shown in Fig. 8.3. The probe output also shows a number of smaller resonance peaks when the probe is in the freestream or in a laminar boundary layer. These resonance peaks are due to vibrations that are a function of the unsupported length of the probe and

vortex shedding from the stem and tip. The pressure fluctuations of the turbulent boundary layer swamp these smaller peaks. The peaks due to vibration of the probe are minimised during the boundary layer survey by placing the probe tip firmly on the surface of the model.

8.2.1 Probe Head and Tip

The length of the probe head is approximately $23\,mm$, to allow tapering of the head as it approaches the tube that forms the tip. The tip is approximately $7\,mm$ long. The OD of the tip is determined from the competing desire to have the entire tip inside the boundary layer, and to maximise the internal diameter (ID) to minimise viscous losses. The Mangler transformation of the Thwaites' method [73] estimates the momentum thickness of a laminar boundary layer at $x_{bc} = 0$ on the axisymmetric spheroid to be $0.057\,mm$ at $Re_l = 4.0 \times 10^6$, using the surface velocity distribution estimated from classical potential theory. If the momentum thickness is assumed to be approximately one eighth of the total boundary layer thickness [53] this implies a boundary layer height of about $0.5\,mm$.

The testing with the spheroid suggested improvements could be made to the probe head design. The initial design continued the internal diameter of the tip through until the end of the probe head (Fig. 8.6). When the probe head and sensor housing where threaded together a discontinuous expansion of the ID into the volume housing the sensor occurred. This sensor volume has a $2.8\,mm$ diameter and is approximately $0.2\,mm$ long, with the entry point opposite the sensor diaphragm. Gradually increasing the internal diameter of the probe head as it approaches the sensor should:

- improve the flow continuity in the vicinity of the sensor when the diaphragm deflects.

- prevent the sensor blocking the hole. The sensor is fixed into the housing using epoxy. If the sensor is not seated correctly the distance between the end of the probe head and sensor diaphragm may be less than desirable. It is suspected that this may have been the cause of some initial problems encountered when developing these probes.

- reduce the effective mass the sensor diaphragm experiences when it deflects and thus increase the natural frequency.

The effective mass experienced by the sensor diaphragm may be calculated from the kinetic energy of the fluid moving with the diaphragm. The mass of fluid in each section of the internal

geometry and its velocity is determined by

$$\begin{aligned} m_{in} &= \pi\ \rho\, r_{in}^2\, l_{in} & w_{in} &= \left(\frac{r_{sen}}{r_{in}}\right)^2 w_{sen} \\ m_{con} &= \pi\ \rho \int_0^{l_{con}} r_{con}^2 dl_z & w_{con} &= \left(\frac{r_{sen}}{r_{con}}\right)^2 w_{sen} \\ m_{sen} &= \pi\ \rho\, r_{sen}^2\, l_{sen} \end{aligned} \tag{8.1}$$

where r is the internal radius, m is the mass of fluid in the section, w is the velocity of fluid in the section, l is the length of each section, and l_z is distance from the narrowest part of the conical section in the axial direction. The subscripts in, con, sen designate the inlet, conical and sensor sections respectively. The internal radius within the conical section is

$$r_{con} = r_{in} + \left(\frac{r_{sen} - r_{in}}{l_{con}}\right) l_z. \tag{8.2}$$

Integrating the kinetic energy of the fluid in the probe head and tip, and then dividing through by $w_{sen}^2/2$, provides an estimate of the effective mass seen by the sensor diaphragm as

$$\begin{aligned} m_{eff} &= \frac{1}{w_{sen}^2}\left(m_{sen}\, w_{sen}^2 + \pi\ \rho \int_0^{l_{con}} (r_{con}\, w_{con})^2\ dl_z + m_{in}\, w_{in}^2\right) \\ &= \frac{\rho\ \pi}{r_{in}^2}\left(r_{sen}^2\, r_{in}^2\, l_{sen} + r_{sen}^3\, r_{in}\, l_{con} + r_{sen}^4\, l_{in}\right) \end{aligned} \tag{8.3}$$

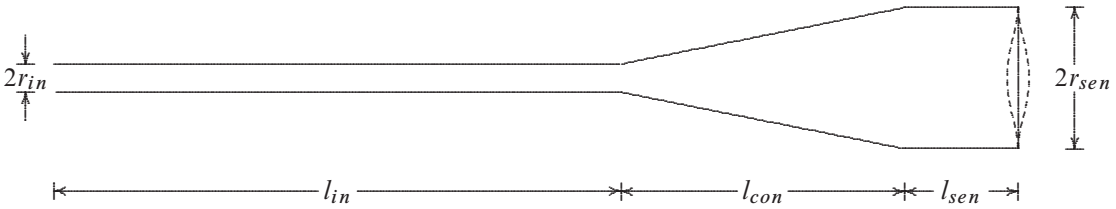

Figure 8.4: Schematic of probe head internal geometry

The first and third terms inside the brackets of Eq. 8.3 determine the effective mass for the sensor and inlet sections respectively. Examining these terms shows the effective mass per unit length of the sensor section is less than that of the inlet provided $r_{sens} > r_{in}$. If considering only the effective mass experienced by the sensor diaphragm it is desirable to maximise the proportion of the internal tube at the diameter of the sensor diaphragm.

An estimate of the diaphragm stiffness may be obtained from the volume displaced under pressure with the assumption of piston like deflection. The first resonant frequency, f_{wd}, due

to the mass of water in the head/tip and the elasticity of the diaphragm may be estimated from

$$f_{wd} = \frac{1}{2\,\pi}\sqrt{\frac{p_{sen_{max}}\,\pi^2\,r_{sen}^4}{\Delta V_{sen_{max}}\,m_{eff}}} \tag{8.4}$$

where $\Delta V_{sen_{max}}$ is the maximum change in the volume V_{sen} when the transducer is subject to its full scale pressure (FSP) rating, $p_{sen_{max}}$. $\Delta V_{sen_{max}}$ is determined from the displacement of the diaphragm under pressure, discarding the assumption of piston like deflection: this is more accurately described as a circular plate with clamped edges. The displacement of such a plate when exposed to a uniform pressure is [74]

$$\begin{aligned} z_{cc}(r_{cc}) &= \frac{3\,p_{sen}\,(1-\nu_P^2)}{16\,E_{sen}\,t_{sen}^3}\left(r_{sen}^2 - r_{cc}^2\right)^2 \\ &= \frac{z_{cc}(0)}{r_{sen}^4}\left(r_{sen}^2 - r_{cc}^2\right)^2 \end{aligned} \tag{8.5}$$

in a cylindrical coordinate system (r_{cc}, θ_{cc}, z_{cc}) with its origin at the centre of the undeflected plate. $z_{cc}(0)$ is the maximum displacement of the sensor diaphragm at $r_{cc} = 0$, ν_P is Poisson's ratio, E_{sen} is the elastic modulus of the sensor diaphragm, and p_{sen} is the static pressure at the sensor. Integration of the displacement with respect to r_{cc} and θ_{cc} determines the change in volume due to the displacement of the sensor diaphragm to be

$$\Delta V_{sen} = \frac{\pi\,z_{cc}(0)\,r_{sen}^2}{3} \tag{8.6}$$

Incidentally this volume is the same as a cone of maximum height $z_{cc}(0)$ with a base radius of r_{sen}. The maximum deflection of this diaphragm should be less than a third of its thickness in order to maintain linearity of better than 5% [75]. The thickness of the diaphragm, t_{sen}, may be estimated from its first resonant frequency in vacuum, f_{dia}, using the results of Mazumdar [76],

$$f_{dia} = \frac{10.215}{2\,\pi\,r_{sen}^2}\sqrt{\frac{E_{sen}\,t_{sen}^2}{12\,\rho_{dia}\,\left(1-\nu_P^2\right)}} \tag{8.7}$$

where ρ_{dia} is the density of the diaphragm, in this case stainless steel ($7700 kg/m^3$). Estimates of the sensor diaphragm's deflection and thickness are obtained using Eq. 8.5, Eq. 8.7, information from the transducer's data sheets and separate correspondence with the manufacturer stating a diaphragm radius of $\approx 1.4 mm$. Table 8.1 details these values and estimates. These estimates ignore the fact that the stated resonant frequencies were obtained at one atmosphere while Eq. 8.7 is valid in a vacuum.

The first resonant frequency increases and the sensitivity (mV/kPa) reduces as the trans-

Full Scale Pressure (kPa)	Resonant Frequency (kHz)	Full Scale Output (mV)	Calculated t_{sen} (μm)	Calculated $z_{cc}(0)$ at Full Scale Pressure (μm)	$\Delta V_{sen_{max}}$ (mm^3)
150	55	50	44	5.8	0.012
350	60	75	48	10.4	0.021
700	70	125	56	13.2	0.027
1500	100	125	80	9.7	0.020

Table 8.1: Properties of pressure sensors suitable for use in FRTPP

ducer full scale pressure increases. The change in the first resonant frequency is expected to be proportionally greater than shown in Table 8.1 when one side of the transducer is adjacent to water (as the mass of the diaphragm is small compared to the effective mass of the water). The increase in full scale voltage with the increased full scale pressure also makes the selection of the transducer with lower sensitivity and hence greater stiffness more attractive. As the accuracy of the pressure measurements is not critical in determining the boundary layer state the $350\,kPa$ transducer was chosen for the boundary layer survey on the ellipsoid. Fig. 8.5 shows the frequency response in a turbulent boundary layer of the probe head with a tapered internal geometry (Fig. 8.6(b)) where $l_{con} = 10\,mm$, $l_{in} = 19\,mm$, $l_{sen} = 0\,mm$, $r_{sen} \approx 1.4\,mm$ and $r_{in} = 0.2\,mm$.

For an inlet with an ID of $0.4\,mm$, a sinusoidal displacement at $1000\,Hz$ with sufficient pressure to create a displacement, ΔV_{sen}, of $0.02\,mm^3$ requires a maximum inlet velocity of $0.5\,m/s$ assuming a slip condition on the walls. This rough estimate suggests that the small diameter inlet will result in significant damping at higher frequencies. This is not necessarily undesirable, as Arndt and Ippen [77] deliberately increased damping to flatten the main resonant peak.

The sensitivity of the f_{wd} (and f_H) estimates to full scale pressure (FSP) rating and inlet tube radius is shown Fig. 8.7, with an increase in r_{in} from $0.20\,mm$ to $0.25\,mm$. Thin-wall hypodermic tubing with a ID and OD of $0.5\,mm$ and $0.7\,mm$ respectively has since been sourced for use with the tips.

The Helmholtz resonance formed by the mass of water in the inlet and the compressibility of the volume adjacent to the sensor must be considered. If any contribution due to the flexibility of the diaphragm is momentarily neglected, the frequency of the Helmholtz resonator, f_H, for

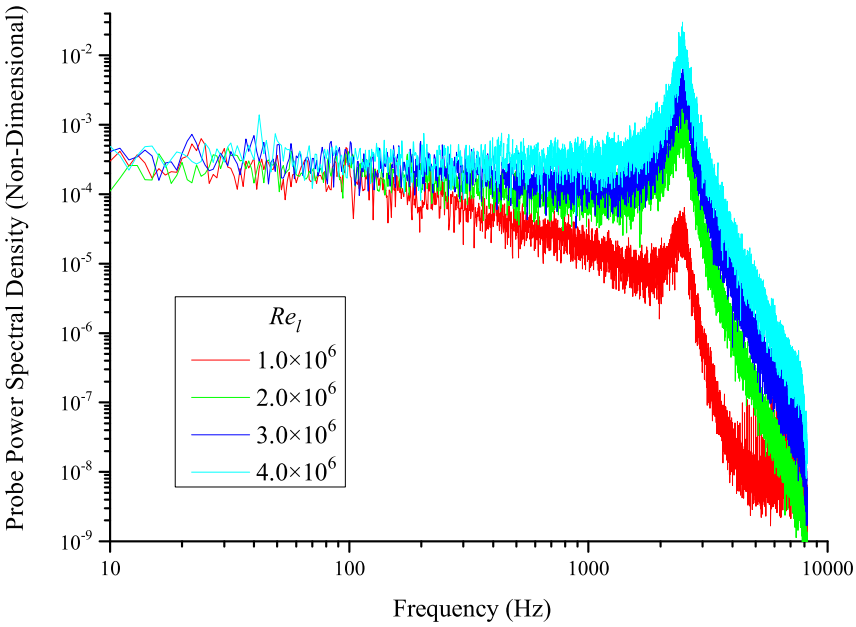

Figure 8.5: Frequency response of FRTPP with $0.7\,mm$ diameter tip, tapered internal section and $350kPa$ transducer in a turbulent boundary layer. ($l_{con} = 10mm$, $l_{in} = 19mm$, $l_{sen} \approx 0\,mm$, $r_{sen} = 1.4\,mm$, and $r_{in} = 0.2\,mm$)

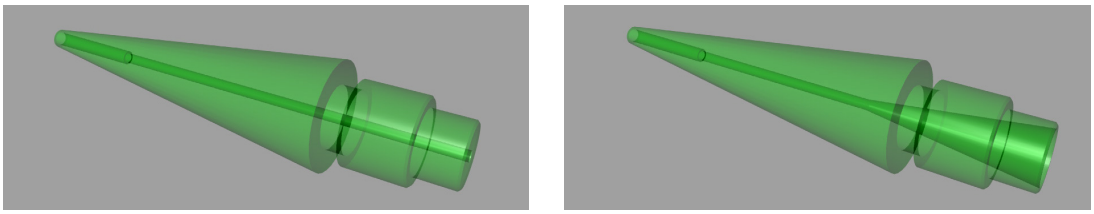

(a) Constant internal diameter

(b) Tapered internal diameter

Figure 8.6: Probe head geometry.

the geometry shown in Fig. 8.4 with $l_{con} = 0$ is

$$f_H = \frac{v_{ss}}{2\pi}\sqrt{\frac{r_{in}^2}{r_{sen}^2\, l_{sen}\, l_{in}}} \tag{8.8}$$

where v_{ss} is the speed of sound in water ($\approx 1500\,m/s$). For $r_{sen} = 1.4\,mm$, $r_{in} = 0.2\,mm$, $l_{sen} = 5\,mm$, and $l_{in} = 25\,mm$ the frequency of the Helmholtz resonator is $\approx 3\,kHz$. This suggests that a Helmholtz type resonance may be of concern and warrants further investigation. The flexibility of the diaphragm contributes to the elasticity experienced by the mass of water in the inlet. Allowing for the diaphragm results in

$$f_H = \frac{v_{ss}}{2\pi}\sqrt{\frac{r_{in}^2}{r_{sen}^2\, l_{sen}\, l_{in}\,(1 + C_{dia})}} \tag{8.9}$$

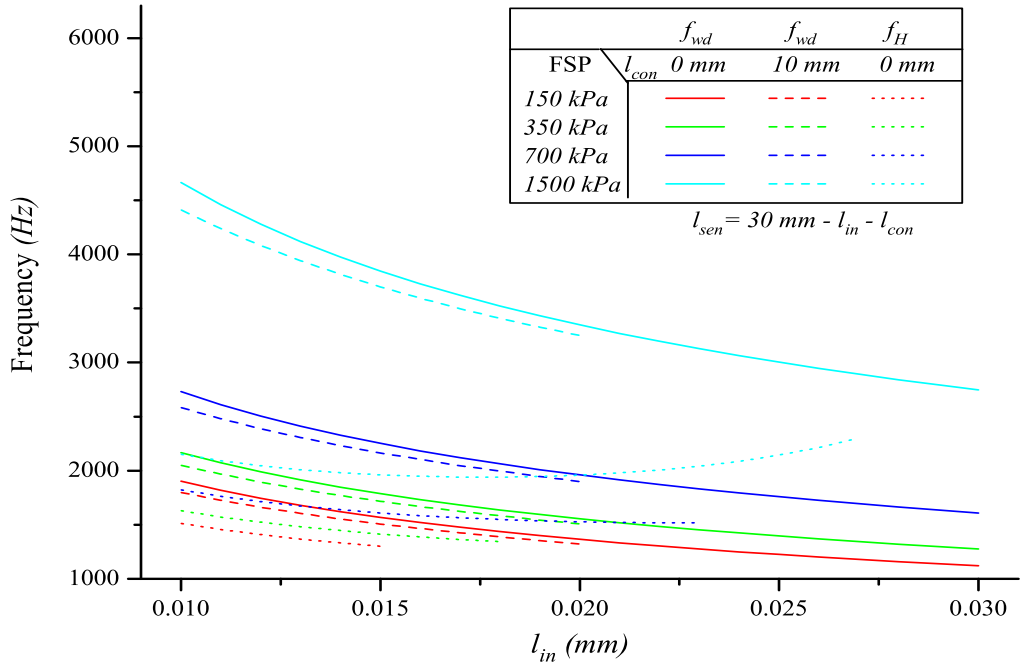

(a) $r_{in} = 0.20\,mm$

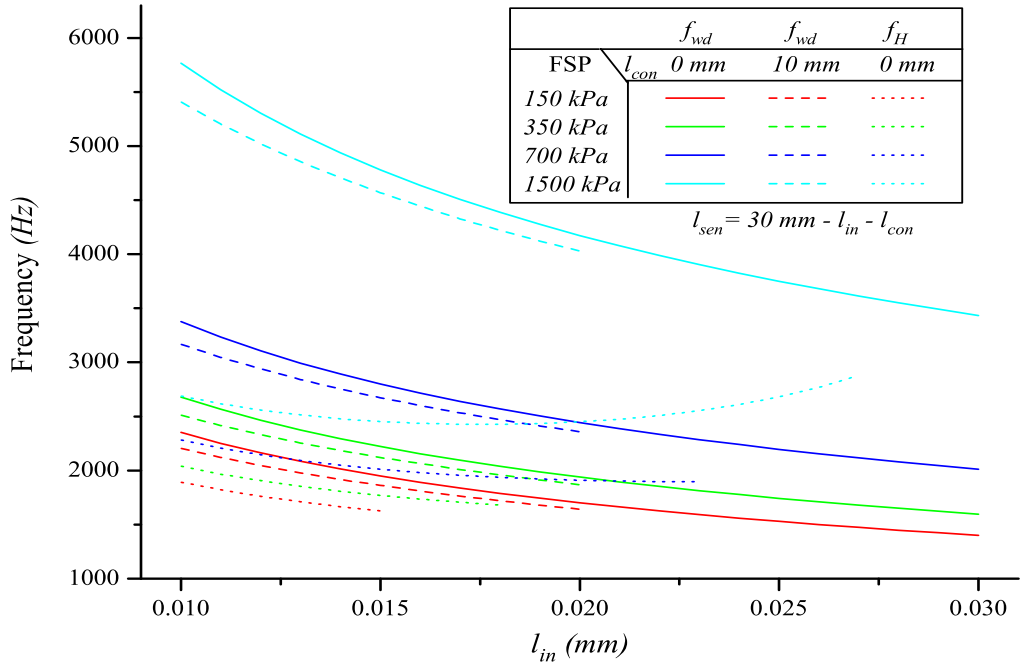

(b) $r_{in} = 0.25\,mm$

Figure 8.7: Calculated first resonant frequency of pressure transducer in the probe head. Using a fixed distance between the probe tip and sensor of $30\,mm$ so the external profile may be tapered, with a minimum $10mm$ length of this low diameter tubing to allow for a short length of tube parallel to the freestream before the 90° bend into the probe tip this figure examines the influence on the first resonant frequency of the diameter of the remaining length of tubing between the tip and sensor. Increasing the length of tubing with the diameter of the sensor reduces the effective mass of the fluid and thus increases f_{wd} however this change in length also influences f_H.(Note: for this figure $r_{sen} = 1.4\,mm$, $K_{bm} = 2.23\,GPa$, $v_{ss} = 1500\,m/s$)

Sensor Full Scale Pressure (kPa)	$l_{sen} = 5\,mm$ $l_{in} = 25\,mm$		$l_{sen} = 10\,mm$ $l_{in} = 20\,mm$		$l_{sen} = 15\,mm$ $l_{in} = 15\,mm$	
	C_{dia}	f_H (Hz)	C_{dia}	f_H (Hz)	C_{dia}	f_H (Hz)
150	5.8	1170	2.9	1220	1.9	1330
350	4.4	1310	2.2	1340	1.5	1440
700	2.8	1570	1.4	1560	0.93	1640
1500	0.96	2180	0.48	1980	0.32	1980

Table 8.2: Influence of sensor diaphragm on Helmholtz resonance (Note: for this table $l_{con} = 0\,mm$, $r_{in} = 0.2\,mm$, $r_{sen} = 1.4\,mm$, $K_{bm} = 2.23\,GPa$, $v_{ss} = 1500\,m/s$)

where C_{dia} is the relative compliance of the diaphragm to that of the water in the volume adjacent to the sensor, V_{sen}.

$$C_{dia} = \frac{K_{bm}\,\Delta V_{sen_{max}}}{V_{sen}\,p_{sen_{max}}} \tag{8.10}$$

where K_{bm} is the bulk modulus (adiabatic) of the water. Table 8.2 shows values for C_{dia} and f_H for a number of sensors with different pressure ranges using the properties in Table 8.1. When $C_{dia} \gg 1$ the elasticity of the diaphragm dominates and the behaviour of the fluid is more accurately considered as the entire mass of water in the head and tip acting on the diaphragm as previously discussed (as this analysis neglects the movement of the mass of water in the volume adjacent to the sensor). When $C_{dia} \not\gg 1$ a Helmholtz resonance may be significant. Fig. 8.7 includes curves showing estimates of f_H when $C_{dia} < 2$. The work of Tang [78] suggests that a tapered inlet, where the taper expands as it approaches the main volume, will marginally increase the frequency of the Helmholtz resonance.

8.2.2 Probe Stem

The surface pressure on a circular cylinder in subcritical flow has a smaller negative excursion ($C_p \approx -1.4$) than one that is supercritical ($C_p \approx -2.2$). The Reynolds number based on the $12\,mm$ diameter probe stem, Re_D, is 27.5 times less than the Reynolds number based on the model length so, Re_D is in the range of 36 000 to 145 000 for the these tests. At these Re_D values the stem is expected to be subcritical. As the maximum freestream tunnel velocity will result in a dynamic pressure of approximately $72\,kPa$ the minimum surface pressure while the stem is subcritical is expected to be greater than the vapour pressure, p_{vap}, of water with the test section at $110\,kPa$. In practice cavitation inception occurred first in the core of the vortices shed from the stem and not on its surface. With the test section at $110\,kPa$ cavitation occurred

at $Re_D = 100\,000$ or a cavitation number, σ_c, of 3.0. The cavitation number is given by

$$\sigma_c = \frac{p_{ref} - p_{vap}}{q_{ref}} \tag{8.11}$$

which is $\approx -C_p$ when $p_{ref} \gg p_{vap}$. The inception cavitation number varied with Reynolds number (e.g. $\sigma_c \approx 2.75$ at $Re_D = 78\,000$). In order to prevent cavitation on the stem the tunnel is pressurised when running at the higher Reynolds numbers. As noted in Section 8.3 the major error in determining the position of the probe relative to the model occurs when the tunnel is pressurised.

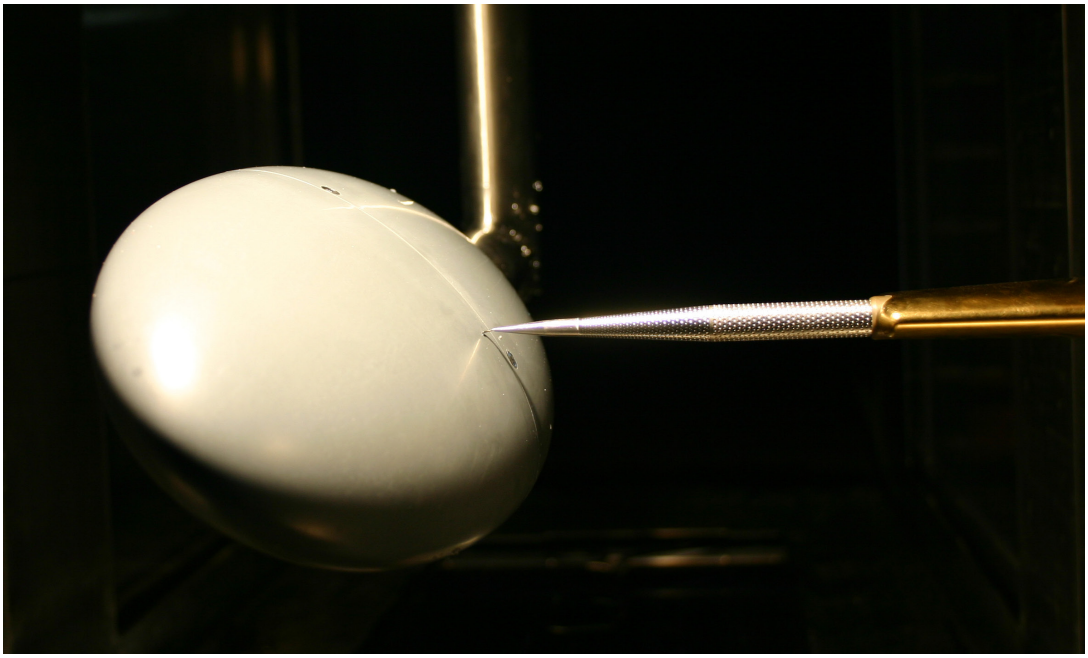

Figure 8.8: Boundary Layer Survey on Ellipsoid. Model rotated 45° about x_t to improve probe access to pressure side. Dimpling the probe allowed a reduction in the test section static pressure required to eliminate cavitation in the wake of the probe.

Cavitation occurred in the wake of the subcritical stem flow at a cavitation number greater than would be experienced on the surface of a supercritical stem. In an effort to reduce the strength of the shed vortices, and thus decrease the inception cavitation number, the surface of the stem and stem adaptor was dimpled to encourage earlier boundary layer transition. This dimpling results in a significant decrease in the inception cavitation number for the probe. After dimpling of the stem and stem adaptor, cavitation was initially observed near the probe head at $\sigma_c \approx 2.2$ at $Re_D = 114\,000$. The reduction in vortex strength was accompanied by reduced overall probe vibration as detected by the measured pressure fluctuations in the freestream, but the high frequency ($> 1000\,Hz$) vibration appeared greater.

The dimples on the stem were $0.11 \pm 0.01\,mm$ deep with a $1\,mm$ radius. A row of dimples was created by placing one every 15° around the circumference of the stem. The next row was offset 7.5° azimuthally and $1.57mm$ axially. This pattern was repeated for the maximum length of exposed stem. This pattern was maintained on the stem adaptor, with the depth, radius, and spacing of the dimples reducing with the stem adaptor diameter (Fig. 8.8).

8.3 Determining Model Position

The position of the model in traverse coordinates is determined by touching the model at a number of locations with the pitot probe and recording these points. The surface of the model can be described by a quadratic function, so the points at which the probe touches the model (neglecting the offset caused by the finite probe size) satisfy the following equation:

$$Ax_{tr}^2 + By_{tr}^2 + Cz_{tr}^2 + Dx_{tr}y_t + Ex_{tr}z_t + Fy_{tr}z_t + Gx_{tr} + Hy_{tr} + Iz_{tr} = 1 \qquad (8.12)$$

where x_{tr}, y_{tr}, z_{tr} are the traverse coordinates and $A, \cdots, I$ are constants. As long as nine or more points on the surface of the body are known it is possible to determine the unknown constants and thus the offset, orientation and size of the spheroid (or ellipsoid). Although this method was simple to implement, results determined for the unknown constants using this solution were sensitive to error in the measurement of the points. This sensitivity is due to Eq. 8.12 also being the equation for a number of different surfaces. A failing in this approach is that it does not use all the information that is available, i.e. that the shape is an ellipsoid with axes of known axes lengths a_e, b_e and c_e. The equation of an ellipsoid with its axes aligned to the Cartesian coordinates x_{bc}, y_{bc}, z_{bc} with an offset (x_0, y_0, z_0) is given by

$$\left(\frac{x_{bc} - x_0}{a_e}\right)^2 + \left(\frac{y_{bc} - y_0}{b_e}\right)^2 + \left(\frac{z_{bc} - z_0}{c_e}\right)^2 = 1 \qquad (8.13)$$

Rotating this by $(\phi_{tr}, \theta_{tr}, \psi_{tr})$ about (z_{tr}, y_{tr}, x_{tr}) respectively provides an equation for the surface of an ellipsoid with known major and minor axes. In order to determine the model's position in traverse coordinates, the orientation $(\phi_{tr}, \theta_{tr}, \psi_{tr})$ and offset (z_0, y_0, x_0) need to be determined. The non-linear equation obtained from the transformation of Eq. 8.13, together with at least six points on the surface of the ellipsoid, may be used to determine the unknowns. The non-linear Levenberg-Marquardt minimisation routine in LabView [79] was modified to handle more than one independent variable to perform the minimisation. In practice about twenty widely spaced points on the surface were measured in order to obtain positioning of the surface to within $0.1\,mm$. For the spheroidal model there is no requirement to solve for the

rotation about the x_{bc} axis.

The position of the model with respect to the traverse needs a small adjustment when the tunnel is pressurised as the side walls of the tunnel tend to deflect outwards under pressure. The greatest deflection occurs at the top of the tunnel where the test section has reduced stiffness due to the large opening for the top window. Removable external supports are used to minimise this deflection.

8.4 Boundary Layer State

The boundary layer is initially laminar at the forward stagnation point. As it moves downstream it may become turbulent. The transition from laminar to turbulent boundary layer flow is described by Emmons [80]. The turbulent boundary layer is characterised by rapid fluctuations in velocity and pressure due to the eddying motion. The start of transition is characterised by short turbulent bursts with rapid velocity and pressure fluctuations. Further downstream the duration and frequency of the turbulent signals increase until the boundary layer is fully turbulent.

Hot films may be placed on the model surface [17], or pressure sensors may be placed flush with the surface or behind pinhole tappings, in order to measure the fluctuations due to turbulence [81]. These two methods have the advantage that they are essentially non-intrusive and allow simultaneous measurements. A disadvantage is that they do not give useful information in regions of separated flow. Each measurement point requires its own transducer and signal conditioning equipment. Hot wire, hot film and pressure probes may be traversed along the surface. These techniques allow for a high density of measurement points. However there are errors associated with the intrusive nature of a physical probe. Regardless of the sensor, a procedure is required to discriminate between periods of laminar and turbulent flow. Hedley and Keffer [82], together with Canepa [83], provide reviews on a number of these techniques. These methods provide the instantaneous intermittency, γ, which has a value of 1 when the boundary layer is turbulent and 0 when laminar. The time averaged intermittency, $\bar{\gamma}$, is given by

$$\bar{\gamma} = \frac{1}{T} \int_0^T \gamma(t)\, dt \tag{8.14}$$

where T is the total sample period and t is time.

The Peak-Valley Counting (PVC) algorithm [84] was used in this work. The detector function was taken as the magnitude of the time derivative of the FRTPP output squared. The PVC algorithm determines that a peak or valley has been found when the local maxima or minima exceed a threshold S. If another peak or valley occurs within the time window, T_w,

the boundary layer is regarded as turbulent for the period between when the threshold was first exceeded and the subsequent peak: accordingly γ is set to 1 for this period. The starting point of the window is brought forward to this next peak and the process is repeated until no peak or valley occurs within the window T_w. On the final peak or valley the turbulent burst is considered to end when the detector function no longer exceeds the threshold. The amplitude of the threshold S and period of time window T_w used with this algorithm were determined experimentally. The threshold amplitude varied between $0.005\,kPa^2/\mu s$ at $Re_l = 2.0\times10^6$ to $0.070\,kPa^2/\mu s^2$ at $Re_l = 4.0\times10^6$. A time window of 900 to 700 μs was used for Re_l between 2.0×10^6 and 4.0×10^6. Examples of the FRTPP output, detector function and PVC algorithm are shown in Fig. 8.9 for a measurement on the spheroid.

For the spheroid no measurements are reported for $\varphi = 0°, -15°, -165°, -180°$ as blockage due to the probe is likely to make these measurements unreliable. For the computational studies the position of the transition at $\varphi = -30°$ will be used for $0°, -15°$; the result at $\varphi = -150°$ will be used for $-165°, -180°$. The problem of blockage due to the probe is more pronounced with the ellipsoid model due to its flattened cross section. In order to minimise this problem, additional keyways machined at $\pm45°$ on the sting allow the model to be rotated about x_t. Using the model at these angles positions either the suction or pressure side of the model towards the probe. This allows measurements to be taken at $\varphi_e = 0°, -15°, -165°, -180°$ with minimal blockage from the probe (Fig. 8.8). It has the disadvantage of requiring two setups for each incidence, placing the models at slightly different positions, and creating a slight change in the angle of the flow as the test section has a 0.2° angle on the flow measured from the top window due to the slope on the test section floor. The boundary layer survey was the only test conducted with the model rotated to these positions.

8.5 Spheroid Boundary Layer Survey Results

The traverse allows 200 mm of travel in the x_t direction. The model position provides probe access from $x_{bc}/l \approx -0.15$ to $x_{bc}/l \approx 0.47$. Measurements are taken every 5 mm in the x_{bc} direction although the length of the traverse is often shortened if a region is not believed to be of interest. A 15° increment is used in the azimuthal direction.

The transition process occurs over a relatively short proportion of the body length (typically 5%). A comparison of $\bar{\gamma}$ for $\alpha = 6°$, $Re_l = 3.0\times10^6$ with Dhawan and Narasimha's [85] distribution of intermittency

$$\bar{\gamma} = 1 - e^{-0.412\,\xi^2}; \quad \xi = \frac{x_{bc} - x_{\bar{\gamma}_{0.00}}}{x_{\bar{\gamma}_{0.75}} - x_{\bar{\gamma}_{0.25}}} \tag{8.15}$$

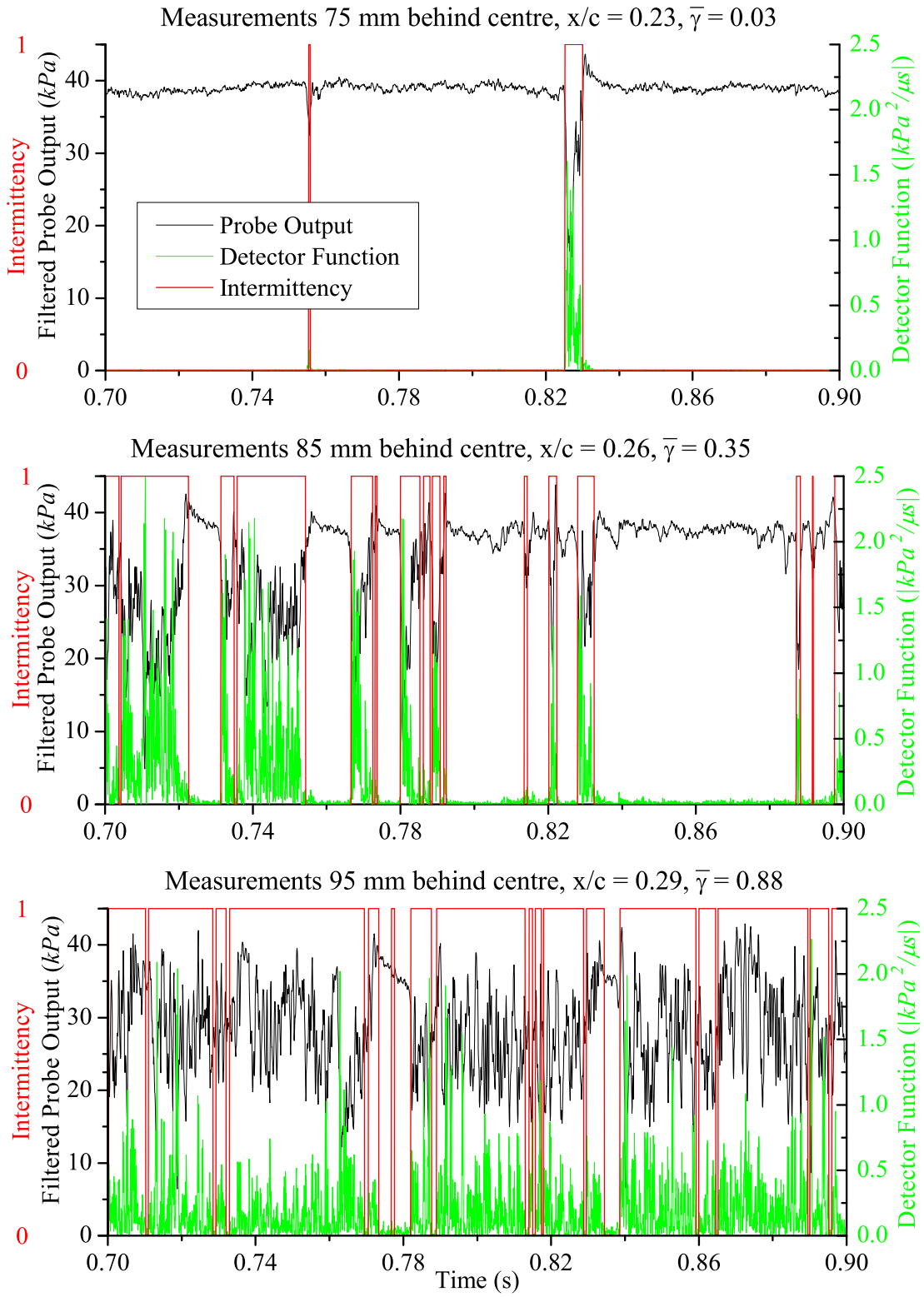

Figure 8.9: Intermittency measurements on spheroid with $0.7mm$ diameter tip, $Re_l = 3.0\times10^6$.

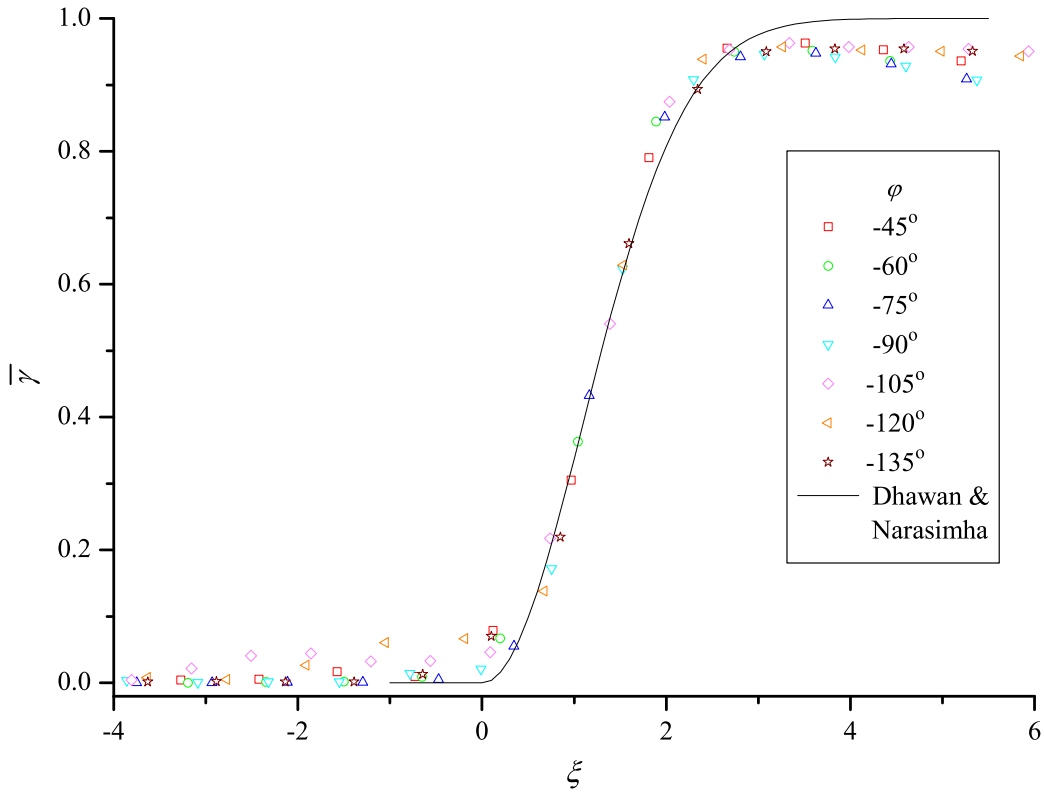

Figure 8.10: Comparison of measured $\bar{\gamma}$ and Eq. 8.15 for the spheroid at $\alpha = -6.2°$, $Re_l = 3.0 \times 10^6$. The reduction in $\bar{\gamma}$ from its maximum value, most apparent for smaller φ and larger ξ, is due to the probe measuring in regions with thicker boundary layers and possibly separated flow.

shows reasonable agreement (Fig. 8.10). $x_{\bar{\gamma}_{0.00}}$ is the axial starting location of transition in body coordinates; other subscripts indicate the location of the corresponding value of intermittency. The deviation between experimental points and Eq. 8.15 near the start of transition is similar to that seen by Gostelow et al. [86] when examining the distribution of intermittency in a range of pressure gradients. The implementation of the PVC method along with the selection of thresholds and time windows chosen resulted in a maximum $\bar{\gamma} \approx 0.96$; this deviation is apparent in Fig. 8.10. The reduction in $\bar{\gamma}$ from its maximum value, most apparent for smaller φ and larger ξ, is due to the probe measuring in regions with thicker boundary layers and possibly separated flow. Compensation is made for the angle between the attached flow and probe.

From the contour plot of $\bar{\gamma}$ versus axial and angular position (e.g. Fig. 8.11) the locations of the contour lines, $\bar{\gamma}_{0.25}$ and $\bar{\gamma}_{0.75}$ are determined . These lines are plotted for a range of Reynolds numbers for $\alpha = -6.2°$ and $-10.2°$ in Fig. 8.13. A comparison of this data for $\alpha = -10.2°$ and the location of boundary layer transition estimated from the surface pressure distribution, x_{trp}, displays similar trends for all but the highest Reynolds number and is shown in Fig. 8.14. The

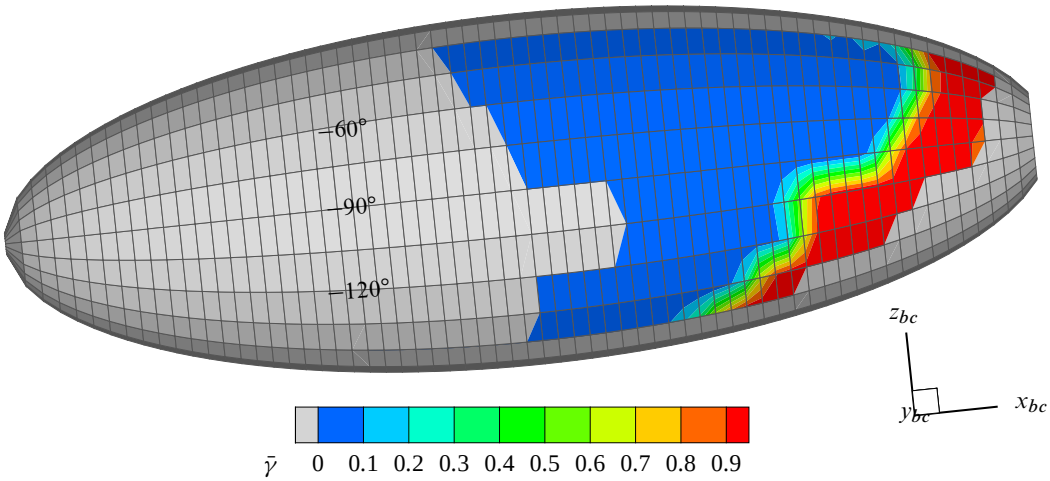

Figure 8.11: Measured time averaged intermittency ($\bar{\gamma}$) for spheroid at $\alpha = -6.2°$, $Re_l = 3.0 \times 10^6$.

estimate from the surface pressure is generally upstream of the location measured using the probe by about $0.1\,l$ to $0.15\,l$ for $Re_l \leq 3.0 \times 10^6$. For $Re_l = 4.0 \times 10^6$ it appears the tappings have caused the boundary layer to transition earlier. The disturbance caused by the tappings may also play a role in the earlier transition at lower Reynolds numbers. A similar trend is seen in the results shown in Table 8.3 for $\alpha = -0.2°$. The results for $\alpha = -0.2°$, $Re_l = 3.0 \times 10^6$ and $\alpha = -10.2°$, $Re_l = 2.0 \times 10^6$ were discarded, as the transition location had shifted forward to a location that was inconsistent with other measurements. The trend of the transition location moving upstream as the Reynolds number increased and in regions of adverse pressure gradient was observed as expected.

The forward shift in transition location is greatest near $\varphi = 100°$ for $\alpha = -6.2°$ and $\alpha = -10.2°$. A potential streamline is calculated through this region for $\alpha = -10.2°$ and the measured values for C_P and $\bar{\gamma}$ are interpolated along this path. These values combined with the azimuthal angle of the streamline are displayed in Fig. 8.12. Assuming the fluid follows the path of the potential streamline, the fluid encounters a steep adverse pressure gradient due to the curvature of the model near $x_{bc}/l = 0.2$; laminar-turbulent transition commences before the steepest of this adverse pressure gradient, after being subject to a region of adverse pressure gradient approximately $0.15\,x_{bc}/l$ long. The adverse pressure gradient (or increasingly adverse pressure gradient) as the flow passes $\varphi = -90°$ towards the suction side is expected to have a significant destabilising influence on any laminar boundary layer.

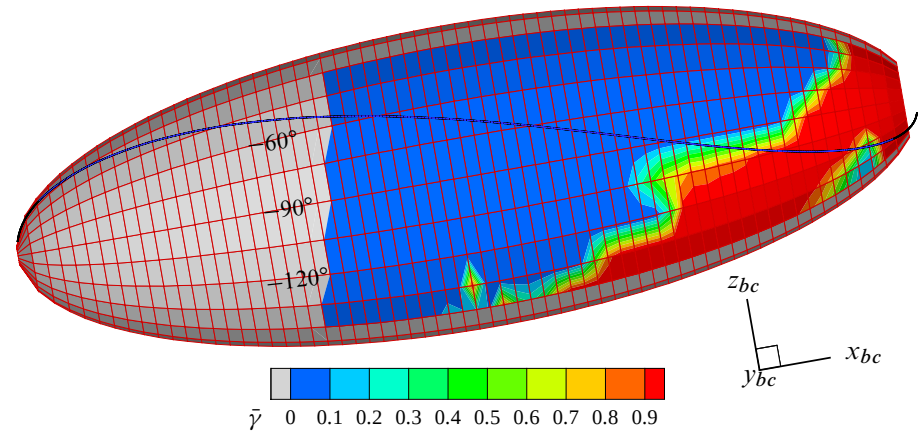

(a) Measured time averaged intermittency ($\bar{\gamma}$)

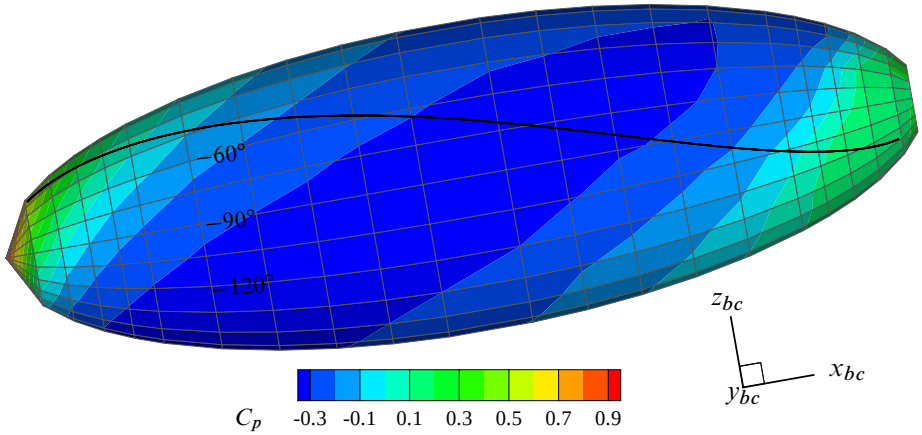

(b) Measured surface pressure distribution (C_p), truncated streamline

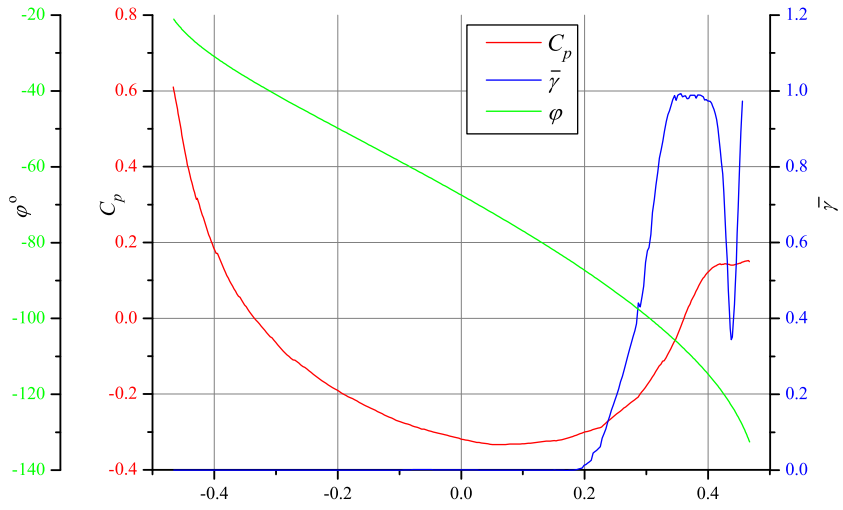

(c) C_p, $\bar{\gamma}$, and φ versus x_{bc}/l

Figure 8.12: Interpolation of measured C_p and $\bar{\gamma}$ for the spheroid along a streamline calculated from classical potential solution, $\alpha = -10.2°$, $Re_l = 3.0 \times 10^6$. The boundary layer starts to become turbulent approximately $0.15\,l$ after first encountering an increasingly adverse pressure gradient.

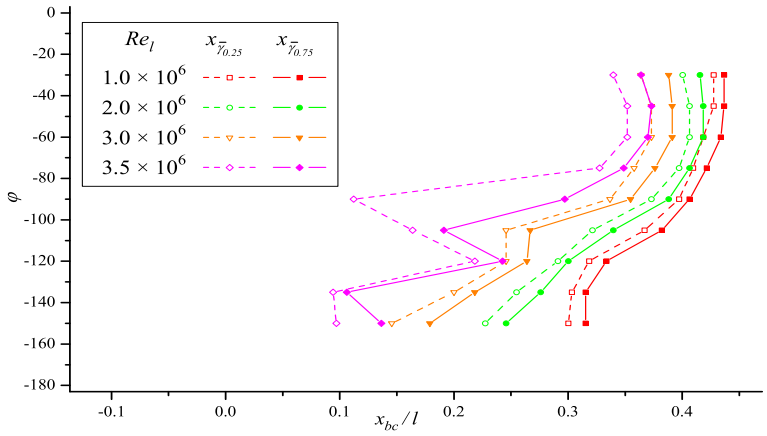

(a) $\alpha = -6.2°$

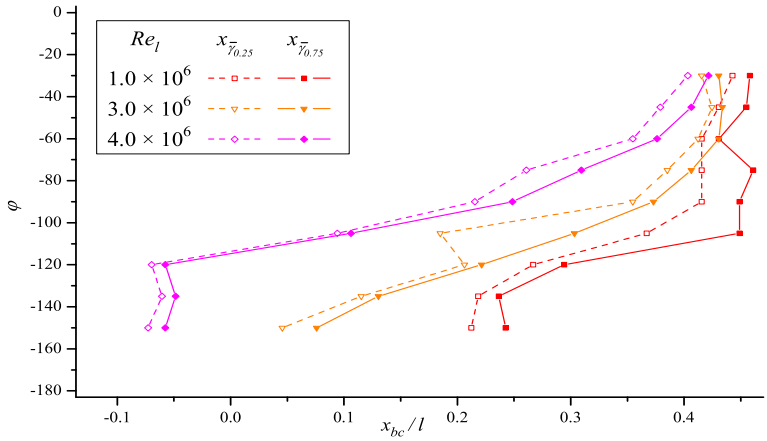

(b) $\alpha = -10.2°$

Figure 8.13: Intermittency measurements on spheroid. These results are used to set the boundary layer state in the calculations presented in Chapter 9.

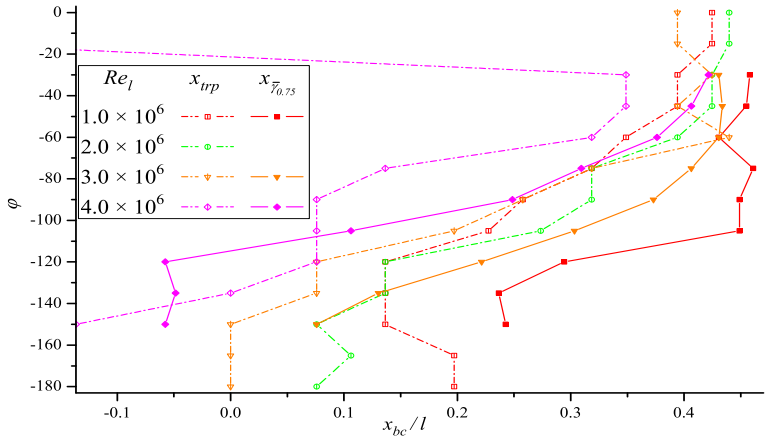

Figure 8.14: Comparison of transition locations on spheroid at $\alpha = -10.2°$ estimated from measured surface pressure distributions, x_{trp}, and 75% intermittency position, $\bar{\gamma}_{0.75}$, derived from the boundary layer survey. The estimate of the location of the boundary layer transition from the surface pressure distributions is generally upstream of the location determined from the boundary layer survey.

Re_l	1.0×10^6			2.0×10^6			3.0×10^6	3.5×10^6		
φ	$\frac{x_{trp}}{l}$	$\frac{x_{\bar{\gamma}_{0.25}}}{l}$	$\frac{x_{\bar{\gamma}_{0.75}}}{l}$	$\frac{x_{trp}}{l}$	$\frac{x_{\bar{\gamma}_{0.25}}}{l}$	$\frac{x_{\bar{\gamma}_{0.75}}}{l}$	$\frac{x_{trp}}{l}$	$\frac{x_{trp}}{l}$	$\frac{x_{\bar{\gamma}_{0.25}}}{l}$	$\frac{x_{\bar{\gamma}_{0.75}}}{l}$
30°	0.36	0.38	0.40	0.32	0.32	0.35	0.32	−0.42	0.20	0.24
90°	0.36	0.40	0.42	0.32	0.35	0.37	0.32	−0.42	0.16	0.18
150°	0.36	0.36	0.38	0.32	0.31	0.33	0.32	−0.42	0.06	0.08

Table 8.3: Estimate of boundary layer transition location on the spheroid for $\alpha = -0.2°$ from surface pressure measurements and position of 25% and 75% intermittency locations determined from the boundary layer survey.

8.6 Ellipsoid Boundary Layer Survey Results

Improved automation of the traverse allowed a decrease in azimuthal interval to $\Delta\varphi_e = 7.5°$ for the ellipsoid boundary layer survey; a $5\,mm$ interval was maintained in the x_{bc} direction. The measurements at $\alpha = 0.2°$ where contaminated for φ_e between $-75°$ and $-90°$. This upstream shift in transition location was initially explained as being associated with the convergence of potential flow streamlines seen in Fig. 7.29. The observations' that the streamwise location of transition is independent of Reynolds number and lies upstream of the convergence of potential streamlines leads to the conclusion that the thin wedge of turbulent boundary layer between $\varphi_e = -75°$ and $-90°$ is due to a fine leak at the mid-body join.[1] In this region the points shown in Fig. 8.15(a) were taken from between $\varphi_e = -90°$ and $-105°$, assuming symmetry. No results were recorded at $Re = 4.0 \times 10^6$ due to a positioning error that required a probe reconstruction. In general it appears that the results at zero incidences, for both the spheroid and ellipsoid, are more susceptible to disturbances triggering premature boundary layer transition. This may be explained by the favourable pressure gradient on the pressure side suppressing disturbances that may lead to boundary layer transition and the earlier transition on the suction side providing a smaller distance over which these unwanted disturbances can occur. Another factor to consider in this observation is that the thinner boundary layer on the pressure side will be more susceptible to surface disturbances, while the thicker boundary layer on the suction side will be less so. The transition location for $Re_l = 4.0 \times 10^6$ at $\alpha = -6.2°$ and $-10.2°$ shows a tendency to shift suddenly upstream on the pressure side. This shift is believed to be associated with minor perturbations, predominantly at the centre join. At $\alpha = -0.2°$ these shifts were seen for $Re_l \geq 3.0 \times 10^6$.

Except as noted above the transition location for the ellipsoid model at all incidences shows

[1] Another survey at this incidence for φ_e between $-90°$ and $-180°$, discarded due to a disturbance near $\varphi_e = -142.5°$, showed a transition location at $\varphi_e = -97.5°$ considerable further downstream ($x_{bc}/l \approx 0.35$) than that seen at $\varphi_e = -82.5°$. Due to (approximate) symmetry the result at these two angles should be similar.

a gradual shift upstream as the Reynolds number increases. It should be recalled from earlier testing that a laminar separation may precede a transition to turbulence. This was observed in the surface pressure measurements at $Re_l = 1.0 \times 10^6$ and in the flow visualisation at $Re = 2.0 \times 10^6$ for $\alpha = -10.2°$ on the pressure side. The forward shift in transition location near $\varphi_e = 100°$ for $\alpha = -6.2°$ and $\alpha = -10.2°$ is more pronounced with the ellipsoid than the spheroid. It is reasonable to assume the ellipsoid's larger adverse azimuthal pressure gradient is responsible.

The comparison of the location measured for $\bar{\gamma}_{0.25}$ using the FRTPP and the location of boundary layer transition estimated from the surface pressure measurements is shown in Fig. 8.16. For $Re_l \leq 2.5 \times 10^6$ the location estimated from the surface pressure measurements is upstream of the location of $\bar{\gamma}_{0.25}$ measured using the FRTPP by around $0.15l$. This is similar to the difference observed between these two measurements over this Reynolds number range for the 3–1 spheroid. The difference may be due to additional disturbance caused by the tapping holes; it is also possible that the influence on the surface pressure caused by boundary layer transition is being detected upstream of the location of transition. For $Re_l \geq 3.5 \times 10^6$ it is believed that disturbance caused by the tappings is causing the location of boundary layer transition to move significantly upstream for a large proportion of the measurement locations.

The $\bar{\gamma}_{0.25}$ curve for the ellipsoid at $\alpha = -6.2°$, $Re_l = 2.5 \times 10^6$ is overlaid on the flow visualisation for the same conditions in Fig. 8.17(a). This figure shows the curve for $\bar{\gamma}_{0.25}$ slightly downstream of the open separation for φ_e between $-75°$ and $-105°$. The convergence of flow onto this separation line creates a divergence of flow near $x_{bc}/l = 0.04$, $\varphi_e = -120°$. This flow divergence should thin the boundary layer between $\varphi_e = -120°$ and $\varphi_e = -150°$, which may account for the delay in transition at this azimuth. Similar behaviour is seen for the $\bar{\gamma}_{0.25}$ curve and the flow visualisation at $Re_l = 2.0 \times 10^6$. This behaviour is apparent to a lesser extent at $\alpha = -6.2°$, $Re_l = 3.0 \times 10^6$, where the flow visualisation shows no open separation line but a general convergence of surface streamlines towards $\varphi_e = -90°$ from $\varphi_e = -110°$ near the midbody. At $\alpha = -6.2°$, $Re_l = 4.0 \times 10^6$ there is no remnant of the open separation divergence of surface streamlines from the region between $\varphi_e = -120°$ and $\varphi_e = -150°$.

It is worth noting at this point that the divergence apparent in the surface streamlines may provide an explanation for the transition occurring further downstream. In Subsection 7.2.2 the presence of transition and the associated increase in shear stress was linked to a deviation in surface streamlines when the transition line and the surface streamlines meet at a small angle (Fig. 7.9).

For $\alpha = -10.2°$, $Re_l = 2.5 \times 10^6$ the $\bar{\gamma}_{0.25}$ curve on the ellipsoid is slightly upstream of the separation on the flank and shifts rapidly upstream in the region of adverse azimuthal pressure

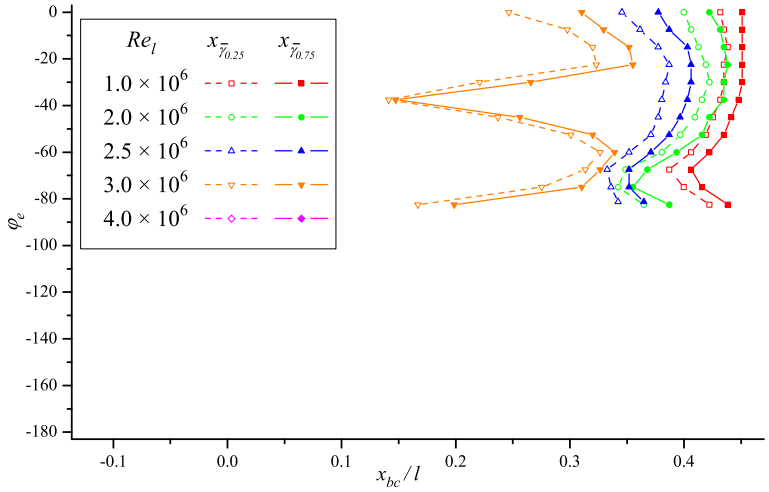

(a) $\alpha = -0.2°$

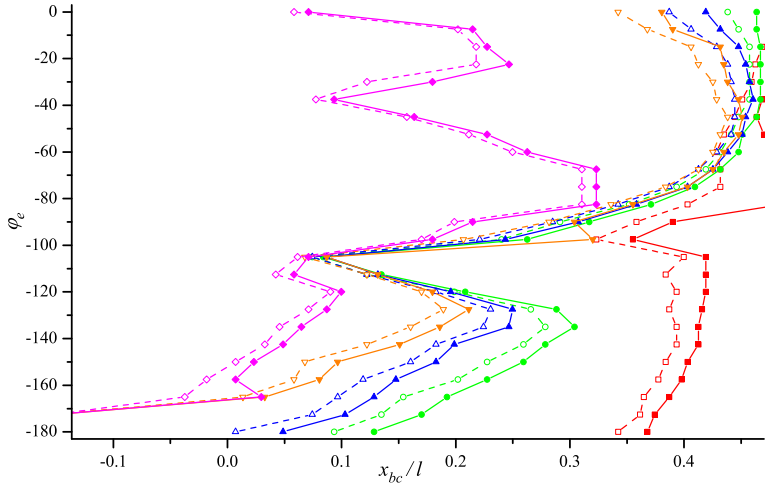

(b) $\alpha = -6.2°$

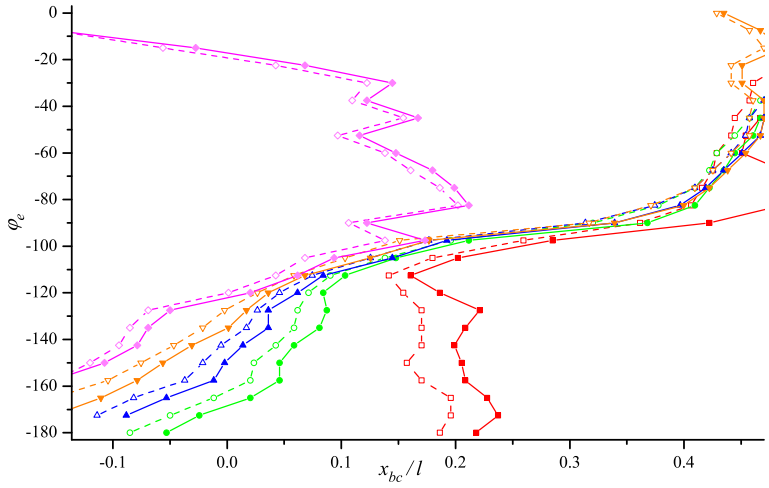

(c) $\alpha = -10.2°$

Figure 8.15: Intermittency measurements on ellipsoid.

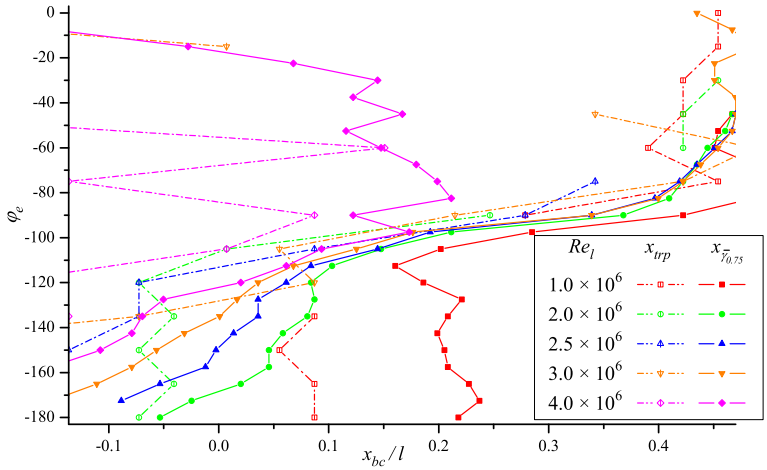

Figure 8.16: Comparison of transition locations on ellipsoid at $\alpha = -10.2°$ estimated from measured surface pressure distributions, x_{trp}, and 75% intermittency position, $\bar{\gamma}_{0.75}$, determined from the boundary layer survey.

gradient. Although a kink in the surface streamlines is apparent at $x_{bc} = 0.0$, $\varphi_e = 100°$ (Fig. 8.17(b)) no general divergence in the surface streamlines is evident as was the case in Fig. 8.17(a) where an open separation was present. The $\bar{\gamma}_{0.25}$ curve has a gradual shift upstream between $\varphi_e = 120°$ and 180°.

8.7 Ellipsoid Wake Survey

Shifting the ellipsoid 150 mm upstream in the x_t direction allowed the traverse to position the FRTPP in the wake of the ellipsoid (but before the support foil). This was then used to measure the total pressure in the y_t–z_t plane. For this survey the FRTPP used a 1.05 mm OD, 0.69 mm ID tip. Results from this survey are presented with those of the CFD in Section 10.3 to allow convenient comparison.

8.8 Summary

A three-dimensional traverse and FRTPP were manufactured along with corresponding electronics and software. These items were used to perform a boundary layer survey on the models. The PVC method was applied to the time derivative of the FRTPP output squared to determine the variation of turbulent intermittency with time, $\gamma(t)$.

The boundary layer transition generally occurs over a small portion of the total model length, in the order of 5%. Narasimha's intermittency function $\gamma(x)$ was found to be a reasonable fit to the measured streamwise intermittency variation $\bar{\gamma}(x)$. Contours of $\bar{\gamma}_{0.25}(\varphi)$ and $\bar{\gamma}_{0.75}(\varphi)$ were

determined from the boundary layer surveys. The position of these curves and Narasimha's intermittency function will be later used to interpolate the intermittency across the mesh used in the computational studies. The location of transition regions except as noted below behave as expected, shifting upstream with increasing Reynolds number and unfavourable pressure gradients.

The boundary layer survey reinforced concerns that at the higher Reynolds numbers the sudden shift forward seen in the transition location estimated from the surface pressure measurements is influenced by the tappings. At lower Reynolds numbers the transition location estimated from the surface pressure measurements displayed similar trends to those obtained from intermittency measurements using the FRTPP, but was generally further upstream by about 10% to 15% of the body length (l).

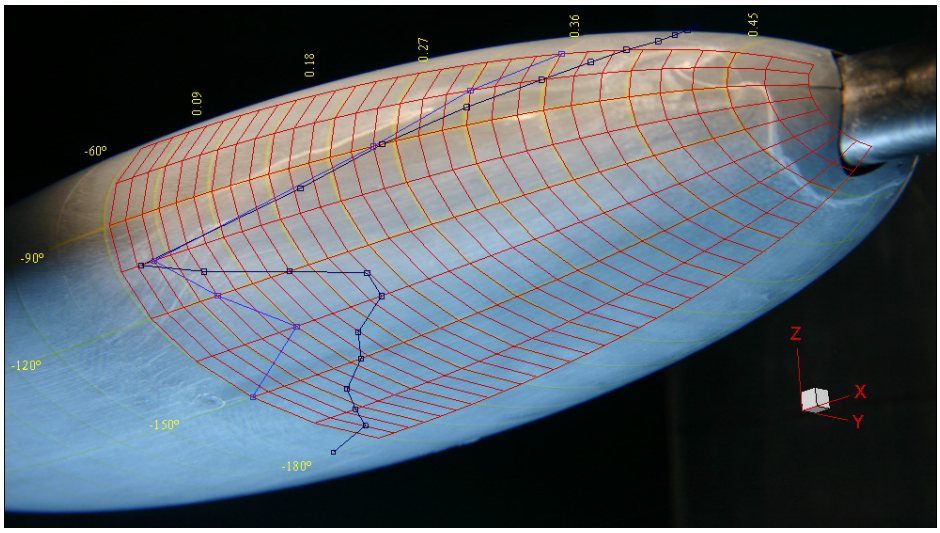

(a) $\alpha = -6.2°$, the convergence of flow onto the open separation line creates a divergence of flow near $x_{bc}/l = 0.04$, $\varphi_e = -120°$ that may be responsible for the later boundary layer transition between $\varphi_e = -120°$ and $\varphi_e = -150°$. Note - The thickening of fluid near the x_{bc}= 0 is seen to move downstream in the sequence of photos.

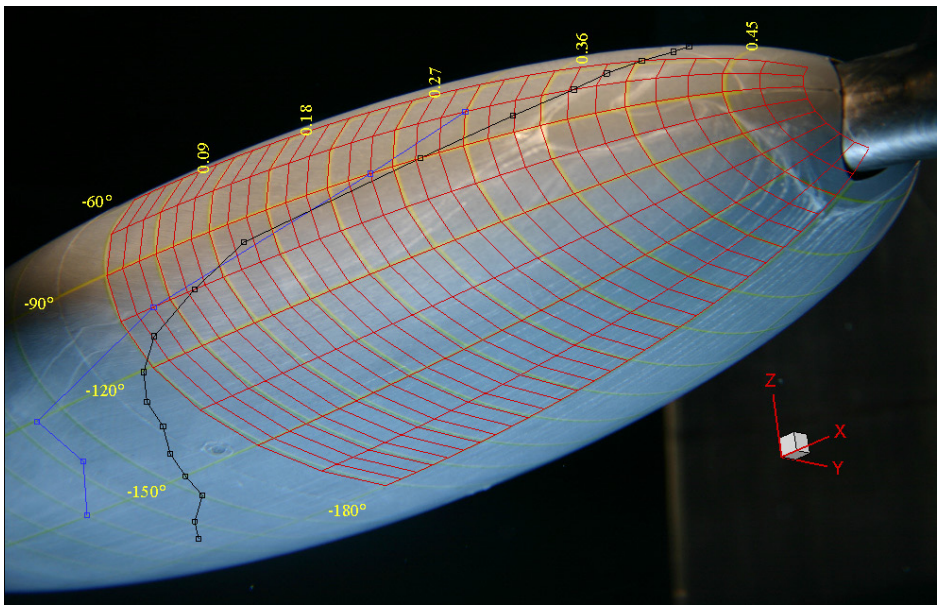

(b) $\alpha = -10.2°$, although a kink in the surface streamlines is apparent at $x_{bc} = 0.0$, $\varphi_e = 100°$ (Fig. 8.17(b)) no general divergence in the surface streamlines is evident as was the case in Fig. 8.17(a)

Figure 8.17: $\bar{\gamma}_{0.25}$ contour (black line) and location of transition estimented from surface pressue measurements (blue) overlayed on surface flow visualisation of ellipsoid, $Re_l = 2.5 \times 10^6$.

Bibliography

[1] Munk, M. M., 1924, "The aerodynamic forces on airship hulls," Tech. rep., National Advisory Committee for Aeronautics, NACA Report 184.

[2] Hopkins, E. J., 1951, "A semi-empirical method for calculating the pitching moment of bodies of revolution at low mach number," Tech. rep., National Advisory Committee for Aeronautics, NACA RM-A51C14.

[3] Fink, R. D., 1976, "USAF stability and control DATCOM," Tech. rep., United States Airforce Flight Dynamics Laboratory.

[4] Fidler, J. E. and Smith, C. A., 1977, "Methods for predicting submersible hydrodynamic characteristics," Tech. rep., Nielsen Engineering and Research Inc., NEAR TR 139.

[5] Peterson, R. S., 1980, "Evaluation of semi-empirical methods for predicting linear static and rotary hydrodynamic coefficients," Tech. rep., Naval Coastal Systems Center, NCSC TM-291-80.

[6] Nahon, M., 1993, "Determination of undersea vehicle hydrodynamic derivatives using the USAF DATCOM," *OCEANS '93*, vol. 2, pp. II/283–II/288.

[7] Funnell, C., ed., 2001, *Janes Underwater Technology*, Jane's Information Group, 4th ed.

[8] Aage, C. and Wagner Smitt, L., 1994, "Hydrodynamic manoeuvrability data of a flatfish type AUV," *OCEANS '94*, vol. 3, pp. III/425–III/430.

[9] Coxhead, M., Graham, P., Neill, R., Price, P., Travers, A., Wharington, J., and Wright, G., 2002, "A report card on Wayamba, DSTO's new uninhabited undersea research vehicle," *UDT Korea 2002*, p. 10 pp.

[10] Guo, J., Tsai, J. F., and Chiu, F. C., 1995, "Design, simulation, and control of a highly maneuverable autonomos underwater vehicle testbed," *MARIENV'95, Tokyo, Japan*, p. 8 pp.

[11] Delery, J. M., 2001, "Robert Legendre and Henri Werle: Toward the elucidation of three-dimensional separation," Annual Review Fluid Mechanics, **33**, pp. 129–154.

[12] Riabouchinsky, D. P., 1921, "On the resistance of spheres and ellipsoids in wind tunnels," Tech. rep., National Advisory Committee for Aeronautics, NACA Report 121, translated from Bulletin of the Aerodynamical Institute of Koutohino.

[13] Eichelbrenner, E. A. and Michel, R., 1958, "Observations sur la transition laminaire-turbulent en trois dimensions," Recherche aeronautique, **65**, pp. 3–10.

[14] Cebeci, T. and Cousteix, J., 1999, *Modeling and Computation of Boundary-Layer Flows*, Horizons Publishing Inc, California.

[15] Han, T. and Patel, V. C., 1979, "Flow separation on a spheroid at incidence," Journal of Fluid Mechanics, **92**, pp. 643–657.

[16] Fu, T. C., Shekarriz, A., Katz, J., and Huang, T. T., 1994, "The flow in the lee of an inclined 6:1 prolate spheroid," Journal of Fluid Mechanics, **269**, pp. 79–106.

[17] Meier, H. U. and Kreplin, H. P., 1980, "Experimental investigation of the boundary-layer transition on a body of revolution," Zeitschrift für Flugwissenschaften und Weltraumforschung, **4**, pp. 65–71.

[18] Kreplin, H. P., Meier, H. U., and Maier, A., 1978, "Wind tunnel model and measuring techniques for the investigation of three-dimensional turbulent boundary layers," *Proceedings of the AIAA 10th Aerodynamic Testing Conference, San Diego, California*, pp. 93–97, paper 78-781.

[19] Cebeci, T., 1978, "Progress in the calculation of three-dimensional laminar and turbulent boundary layers on bodies of revolution at incidence," *Proceedings of the 7th US/FRG DEA-Meeting, AFFDL-TR-78-111*, pp. 237–246.

[20] Meier, H. U., Kreplin, H. P., and Vollmers, H., 1983, "Development of boundary layers and separation patterns on a body of revolution at incidence," *2nd Symposium on Numerical and Physical Aspects of Aerodynamic Flows, State University, Long Beach, California*, T. Cebeci, ed., p. 9.

[21] Vollmers, H., Kreplin, H. P., and Meier, H. U., 1983, "Separation and vortical-type flow around a prolate spheroid - evaluation of relevant parameters," *AGARD CP-342*, pp. 14–1 – 14–14.

[22] Meier, H. U., Michel, U., and Kreplin, H. P., 1987, "The influence of wind tunnel turbulence on the boundary layer transition," *Perspectives in Turbulence Studies, International Symposium DFVLR Research Center*, pp. 26–46.

[23] Kreplin, H. P. and Stäger, R., 1993, "Measurements of the Reynolds-stress tensor in the three-dimensional boundary layer of an inclined body of revolution," *Ninth Symposium on Turbulent Shear Flows, Department of Mechanical Engineering, Kyoto., Japan*, F. Durst et al., eds., pp. 2–4–1 – 2–4–6.

[24] Wetzel, T. G., 1996, *Unsteady Flow Over a 6:1 Prolate Spheroid*, Ph.D. thesis, Virginia Polytechnic Institute and State University, Virginia.

[25] Barber, K. M. and Simpson, R. L., 1991, "Mean velocity and turbulence measurements of flow around a 6:1 prolate spheroid," AIAA Paper 91-0255, p. 10.

[26] Ahn, S., 1992, *An Experimental study of flow over a 6 to 1 prolate spheroid at incidence*, Ph.D. thesis, Virginia Polytechnic Institute and State University, Virginia.

[27] Chesnakas, C. J. and Simpson, R. L., 1994, "Full three-dimensional measurements of the cross-flow separation region of a 6:1 prolate spheroid," Experiments in Fluids, **17**(1), pp. 68–74.

[28] Chesnakas, C. J. and Simpson, R. L., 1996, "Measurements of the turbulence structure in the vicinity of a 3-D separation," ASME Journal of Fluids Engineering, **118**(2), pp. 268–275.

[29] Chesnakas, C. J. and Simpson, R. L., 1997, "Detailed investigation of the three-dimensional separation about a 6:1 prolate spheroid," AIAA Journal, **35**(6), pp. 990–999.

[30] Wetzel, T. G., Simpson, R. L., and Cheesnakas, C. J., 1998, "Measurement of three-dimensional crossflow separation," AIAA Journal, **36**(4), pp. 557–564.

[31] Goody, M., 1999, *An experimental investigation of pressure fluctuations in three-dimensional turbulent boundary layers.*, Ph.D. thesis, Virginia Polytechnic Institute and State University, Virginia.

[32] Granlund, K., 2009, *Steady and unsteady maneuvering forces and moments on slender bodies*, Ph.D. thesis, Virginia Polytechnic Institute and State University, Virginia.

[33] DeMoss, J. A., 2007, *Drag measurements on an ellipsoidal body*, Master's thesis, Virginia Polytechnic Institute and State University, Virginia.

[34] Lamb, S. H., 1932, *Hydrodynamics*, Cambridge University Press, sixth ed.

[35] Milne-Thomson, L. M., 1968, *Theoretical Hydrodynamics*, MacMillan Press Ltd, London, fifth ed.

[36] Band, E. G. and Payne, P. R., 1980, "The pressure distribution on the surface of an ellipsoid in inviscid flow," Aeronautical Quarterly, pp. 70–84.

[37] Wang, K. C., 1970, "Three-dimensional boundary layer near the plane of symmetry of a spheroid at incidence," Journal of Fluid Mechanics, **43**, pp. 187–209.

[38] Wang, K. C., 1975, "Boundary layer over a blunt body at low incidence with circumferential flow," Journal of Fluid Mechanics, **72**, pp. 49–65.

[39] Patel, V. C. and Choi, D. H., 1979, "Calculation of three-dimensional laminar and turbulent boundary layers on bodies of revolution at incidence," *2nd Symposium on Turbulent Shear Flows, Imperial College London*, L. J. S. Bradbury et al., eds., pp. 15.14–15.24.

[40] Cebeci, T., Khattab, A. K., and Stewartson, K., 1980, "On nose separation." Journal of Fluid Mechanics, **97**, pp. 435–454.

[41] Cebeci, T. and Su, W., 1988, "Separation of three-dimensional laminar boundary layers on a prolate spheroid," Journal of Fluid Mechanics, **191**, pp. 47–77.

[42] Cebeci, T., Chen, H. H., Arnal, D., and Huang, T. T., 1991, "Three-dimensional linear stability approach to transition on wings and bodies of revolution at incidence," AIAA Journal, **29**(12), pp. 2077–2085.

[43] Patel, V. C. and Baek, J. H., 1985, "Boundary layers and separation on a spheroid at incidence," AIAA Journal, **23**(1), pp. 55–63.

[44] Rosenfeld, M., Israeli, M., and Wolfshtein, M., 1988, "Numerical study of the skin friction on a spheroid at incidence," AIAA Journal, **26**(2), pp. 129–136.

[45] Rosenfeld, M., Wolfshtein, M., and Israeli, M., 1992, "A numerical study of the laminar incompressible flow over a 6-1 prolate spheroid at incidence," International Journal for Numerical Methods in Fluids, **15**(2), pp. 147–173.

[46] Gee, K., Cummings, R. M., and Schiff, L. B., 1992, "Turbulence model effects on separated flow about a prolate spheroid," AIAA Journal, **30**(3), pp. 655–664.

[47] Constantinescu, G. S., Pasinato, H., Wang, Y., Forsythe, J. R., and Squires, K. D., 2002, "Numerical investigation of flow past a prolate spheroid," Journal of Fluids Engineering, **124**, pp. 904–910.

[48] Kim, S. E., Rhee, S. H., and Cokljat, D., 2003, "Application of modern turbulence models to vortical flow around a 6:1 prolate spheroid at incidence," AIAA Paper 2003-429, p. 11.

[49] Wilcox, D. C., 1998, *Turbulence Modeling for CFD*, D C W Industries Inc., California.

[50] Wikström, N., Svennberg, U., Alin, N., and C., F., 2004, "Large eddy simulation of the flow around an inclined prolate spheroid," Journal of Turbulence, **5**(1), p. 18.

[51] Karlsson, A. and Fureby, C., 2009, "LES of the flow past a 6:1 prolate spheroid." *47th AIAA Aerospace Sciences Meeting including The New Horizons Forum and Aerospace Exposition, Orlando, Florida*, p. 13, paper AIAA-2009-1616.

[52] Brandner, P. A. and Walker, G. J., 2007, "An experimental investigation into the performance of a flush water-jet inlet," Journal of Ship Research, **51**(1), p. 21.

[53] Hoerner, S. F., 1965, *Fluid-Dynamic Drag*, Hoerner Fluid Dynamics, New Jersey, second ed.

[54] Blevins, R. D., 1979, *Formulas for natural frequency and mode shapes*, Krieger Publishing Company, Malabar, Florida.

[55] Meier, H. U. and Kreplin, H. P., 1978, "Pressure distributions and flow visualisations on an ellipsoid 1:6 designed for three-dimensional boundary layer investigations," *Proceedings of the 7th US/FRG DEA-Meeting AFFDL-TR-78-111*, A. W. Fiore, ed., pp. 197–208.

[56] Bevington, P. R. and Robinson, D. K., 2003, *Data Reduction and error analysis for the physical sciences*, McGraw-Hill, New York, third ed.

[57] Cousteix, J. and Pailhas, G., 1979, "Exploratory study of a laminar-turbulent transition process close to laminar boundary layer separation," Recherche Aerospatiale - English, **3**, pp. 79–85.

[58] Brawslow, A. L. and Knox, E. C., 1958, "Simplified method for determination of critical height of distributed roughness particles for boundary-layer transition at Mach numbers from 0 to 5," Tech. rep., National Advisory Committee for Aeronautics, NACA TN 4363.

[59] Barlow, J. B., Rae, W. H., and Pope, A., 1999, *Low-Speed Wind Tunnel Testing*, John Wiley & Sons, New York, third ed.

[60] Von Doenhoff, A. E. and Horton, E. A., 1958, "A low-speed experimental investigation of the effect of a sandpaper type roughness on boundary-layer transition," Tech. rep., National Advisory Committee for Aeronautics, NACA Report 1349.

[61] Panaaras, A. G. and Steger, J. L., 1988, "A thin-layer solution of the flow about a prolate spheroid," Zeitschrift für Flugwissenschaften und Weltraumforschung, **12**, pp. 173–180.

[62] ATI Industrial Automation, 2003, *ISA F/T-16 Intelligent Multi-axis Force/Torque Sensor System, Installation and operation manual*.

[63] Tobak, M. and Peake, D. J., 1982, "Topology of three-dimensional separated flows," Annual Review Fluid Mechanics, **14**, pp. 61–85.

[64] Perry, A. E. and Chong, M. S., 1987, "A description of eddying and flow patterns using critical-point concepts," Annual Review Fluid Mechanics, **19**, pp. 125–155.

[65] Wang, K. C., 1974, "Boundary layer over a blunt body at high incidence with an open type separation," Proceedings of the Royal Society A, **340**, pp. 33–35.

[66] Simpson, R. L., 1968, "Aspects of turbulent boundary layer separation," Progress in Aerospace Sciences, **6**(3), pp. 543–545.

[67] Wu, J. K., Trammel, R. W., Zhu, F. L., and Yin, X. Y., 2000, "Boundary layer over a blunt body at high incidence with an open type separation," Physics of Fluids, **12**(8), pp. 1932–1954.

[68] Squire, L. C., 1961, "The motion of a thin sheet oil sheet under the steady boundary layer on a body," Journal of Fluid Mechanics, **11**, pp. 161–179.

[69] LightHill, M. J., 1963, *Laminar Boundary Layers.*, chap. II - Boundary Layer Theory, Oxford Clarendon Press, pp. 46–113.

[70] Biagioni, L. and d'Agostino, L., 1999, "Measurement of energy spectra in weakly compressible turbulence." 17th AIAA Applied Aerodynamics Conference, AIAA 99-3516, p. 8.

[71] Bradshaw, P., 1971, *An Introduction to Turbulence and its Measurement.*, Pergamon Press, New York.

[72] Brandner, P. A., Clarke, D. B., and Walker, G. J., 2004, "Development of a fast response pressure probe for use in a cavitation tunnel." *15th Australasian Fluid Mechanics Conference*, B. M. et al., eds., p. 4.

[73] Cebeci, T. and Cousteix, J., 1999, *Modeling and computation of boundary-layer flows*, Horizons Publishing Inc., Long Beach, California.

[74] Timoshenko, S. and Woinowsky-Krieger, S., 1959, *Theory of plates and shells*, McGraw-Hill Book Company, New York.

[75] Sirohi, R. S. and Radha Krishna, H. C., 1991, *Mechanical measurements*, Wiley, John & Sons, third ed.

[76] Mazumdar, J., 1971, "Transverse vibration of elastic plates by the method of constant deflection lines." Journal of Sound and Vibration, **18**(2), pp. 147–155.

[77] Arndt, R. E. A. and Ippen, A. T., 1970, "Turbulence measurements in liquids using an improved total pressure probe." Journal of Hydraulic Research, **8**(2), pp. 131–158.

[78] Tang, S. K., 2005, "On helmholtz resonators with tapered necks." Journal of Sound and Vibration, **279**, pp. 1085–1096.

[79] National Instruments Corporation, 2000, *LabVIEW VIs and Functions*.

[80] Emmons, H. W., 1951, "The laminar-turbulent transition in a boundary layer - part 1." Journal of the Aeronautical Sciences, **18**(7), pp. 490–498.

[81] Bull, M. K., 1996, "Wall-pressure fluctuations beneath turbulent boundary layers: Some reflections on forty years of research." Journal of Sound and Vibration, **190**(3), pp. 299–315.

[82] Hedley, T. B. and Keffer, J. F., 1974, "Turbulent/non-turbulent decisions in an intermittent flow." Journal of Fluid Mechanics, **64**, pp. 625–644.

[83] Canepa, E., 2002, "Experiences in the application of intermittency detection techniques to hot-film signals in transitional boundary layers." *The 16th Symposium on Measuring Techniques in Transonic and Supersonic Flow in Cascades and Turbomachines*, p. 10.

[84] Solomon, W. J., 1996, *Unsteady Boundary Layer Transition on Axial Compressor Blades.*, Ph.D. thesis, University of Tasmania.

[85] Dhawan, S. and Narasimha, R., 1958, "Some properties of boundary layer flow during the transition from laminar to turbulent motion," Journal of Fluid Mechanics, **3**(4), pp. 418–436.

[86] Gostelow, J. P., Blunden, A. R., and Walker, G. J., 1994, "Effect of free-stream turbulence and adverse pressure gradients on boundary layer transition," Journal of Turbomachinery, **116**, pp. 392–404.

[87] White, F. M., 1991, *Viscous fluid flow*, McGraw-Hill Inc., New York.

[88] Dryden, H. L., Schubauer, G. B., Mock, W. C., and Skramstad, H. K., 1937, "Measurements of intensity and scale of wind-tunnel turbulence and their relation to the critical

reynolds number of spheres," Tech. rep., National Advisory Committee for Aeronautics, NACA Report 581.

[89] Spangler, J. G. and Wells, C. S., 1998, "Effects of freestream disturbances on boundary-layer transition." AIAA Journal, **36**(4), pp. 557–564.

[90] Drela, M. and Giles, M. B., 1987, "Viscous-inviscid analysis of transonic and low reynolds number airfoils," AIAA Journal, **25**(10), pp. 134–1355.

[91] Stock, H. W., 2006, "Navier-Stokes airfoil computations with e^N transition prediction including transitional flow regions," AIAA Journal, **44**(1), pp. 108–118.

[92] Langtry, R. B., Menter, F. R., Likki, S. R., Suzen, P. G., Y. B.and Huang, and Völker, 2004, "A correlation-based transition model using local variables part II - test cases and industrial applications," *Proceedings of ASME Turbo Expo 2004*, p. 11.

[93] Menter, F. R., Langtry, R. B., Likki, S. R., and Suzen, P. G., Y. B.and Huang, 2004, "A correlation-based transition model using local variables part I - model formulation," *Proceedings of ASME Turbo Expo 2004*, p. 11.

[94] Fluent Inc., 2005, *Fluent 6.2 Users Guide*.

[95] Kim, S. E., Choudhury, D., and Patel, B., 1999, "Computations of complex turbulent flows using the commercial code Fluent," *Modeling complex turbulent flows*, M. D. Salas et al., eds., Kluwer Academic Publishers, pp. 259–276.

[96] Menter, F. R., 1994, "Two-equation eddy-viscosity turbulence models for engineering applications," AIAA Journal, **32**(8), pp. 1598–1604.

[97] Jongon, T., 1998, *Simulation and modeling of turbulent incompressible fluid flows*, Ph.D. thesis, EPF Lausanne, Lausanne, Switzerland.

[98] Jongen, T. and Marx, Y. P., 1997, "Design of an unconditionally stable, positive scheme for the k-ε and two-layer turbulence models," Computers & Fluids, **26**(5), pp. 469–487.

[99] Lighthill, M. J., 1958, "On displacement thickness," Journal of Fluid Mechanics, **4**, pp. 383–392.

[100] Morini, L., Chen, L.-T., and Suciu, E. O., 1975, "Steady and oscillatory subsonic and supersonic aerodynamics around complex configurations," AIAA Journal, **13**(3), pp. 368–374.

[101] Popov, A. V., Botez, R. M., and Labib, M., 2008, "Transition point detection from surface pressure distribution for control design," Journal of Aircraft, **45**(1), pp. 23–28.

[102] Clarke, D. B., Brandner, P. A., and Walker, G. J., 2007, "Computational and experimental investigation of flow around a 3-1 prolate spheroid," *16th Australasian Fluid Mechanics Conference*, P. Jacobs et al., eds., pp. 1381–1387.

[103] Curle, N., 1967, "A two-parameter method for calculating the two-dimensional incompressible laminar boundary layer," Journal of the Royal Aeronautical Society, **71**, pp. 117–123.

[104] Stock, H. W. and Haase, W., 2000, "Navier-Stokes airfoil computations with e^N transition prediction including transitional flow regions," AIAA Journal, **38**(11), pp. 2059–2066.

[105] Head, M. R. and Hayasi, N., 1967, "Approximate calculations of the incompressible laminar boundary layer," The Aeronautical Quarterly, **18**, pp. 259–272.

[106] Stock, H. W., 1980, "Laminar boundary layers on inclined ellipsoids of revolution," Zeitschrift für Flugwissenschaften und Weltraumforschung, **4**, pp. 217–224.

[107] Willmarth, W. W., 1975, "Pressure fluctuations beneath turbulent boundary layers," Annual Review Fluid Mechanics, **7**, pp. 13–38.

[108] Schlichting, H. and Gersten, K., 2000, *Boundary Layer Theory*, Springer-Verlag, Berlin, eighth ed.

[109] Dress, D., 1990, "Drag measurements on a modified prolate spheroid using a magnetic suspension and balance system," Journal of Aircraft, **27**(6), pp. 523–528.

[110] Costi, S. and Portnoy, H., 1974, "Incompressible, inviscid, symmetrical flow about ellipsoids - comparison of an approximate theory with exact results," Scientific Report 5, Department of Aeronautical Engineering, Technion - Israel Institute of Technology.

[111] Hobson, E. W., 1931, *The theory of spherical and ellipsoidal harmonics*, Cambridge University Press, London.

[112] Carlson, B. C., 1995, "Numerical computation of real or complex elliptic integrals," Numerical Algorithms, **10**, pp. 13–26.

[113] The Numerical Algorithms Group Limited, Oxford, 1994, *NAG C Library Manual, Mark 3*, vol. 3.